Frequency Domain Thermoreflectance (FDTR) Instrumentation: Common Challenges and Practical Guidance

Dylan J. Kirsch[1], Joshua Martin[1], Ronald Warzoha[2], Mark McLean[1], Donald Windover[1], Ichiro Takeuchi[3]

[1] Material Measurement Laboratory, National Institute of Standards and Technology, Gaithersburg, MD 20899

[2] Department of Mechanical and Nuclear Engineering, United States Naval Academy, Annapolis, MD 21402

[3] Department of Materials Science and Engineering, University of Maryland, College Park, MD 20742

October 29th, 2024

ITCC & ITES 2024 Conference, Charlottesville, VA

NIST MATERIAL MEASUREMENT LABORATORY

Outline

- Introduction to FDTR
- FDTR Setup & Measurement procedure
- Sensitivity & Spot size measurement
- **Sample Focusing & Camera Alignment**
- **Alignment through objective**
- **Alignment into detector**
- **Electronics & Noise**
  - Mitigation
  - Lock-in settings
  - **Phase noise & Standard Deviation**
- **Model fitting & Monte Carlo simulation**
  - numerical integration studies
  - Uncertainty

NIST FDTR Instrument

Certain commercial equipment, instruments, or materials are identified in this document. Such identification does not imply recommendation or endorsement by the National Institute of Standards and Technology, nor does it imply that the products identified are necessarily the best available for the purpose.

FDTR Instrument Guide Now Available!

An instrumentation guide to measuring thermal conductivity using frequency domain thermoreflectance (FDTR)

Cite as: Rev. Sci. Instrum. 95, 103006 (2024); doi: 10.1063/5.0213738
Submitted: 12 April 2024 • Accepted: 19 September 2024 •
Published Online: 14 October 2024

View Online Export Citation CrossMark

Dylan J. Kirsch,[1,2,a] Joshua Martin,[1,b] Ronald Warzoha,[3,c] Mark McLean,[1,d] Donald Windover,[1,e] and Ichiro Takeuchi[2,f]

AFFILIATIONS

[1] Material Measurement Laboratory, National Institute of Standards and Technology, Gaithersburg, Maryland 20899, USA
[2] Department of Materials Science and Engineering, University of Maryland, College Park, Maryland 20742, USA
[3] Department of Mechanical and Nuclear Engineering, United States Naval Academy, Annapolis, Maryland 21402, USA

[a] **Author to whom correspondence should be addressed:** dylan.kirsch@nist.gov
[b] joshua.martin@nist.gov
[c] warzoha@usna.edu
[d] mark.mclean@nist.gov
[e] donald.windover@nist.gov
[f] takeuchi@umd.edu

ABSTRACT

Frequency Domain Thermoreflectance (FDTR) is a versatile technique used to measure the thermal properties of thin films, multilayer stacks, and interfaces that govern the performance and thermal management in semiconductor microelectronics. Reliable thermal property measurements at these length scales (≈10 nm to ≈10 μm), where the physics of thermal transport and phonon scattering at interfaces both grow in complexity, are increasingly relevant as electronic components continue to shrink. While FDTR is a promising technique, FDTR instruments are generally home-built; they can be difficult to construct, align, and maintain, especially for the novice. Our goal here is to provide a practical resource beyond theory that increases the accessibility, replicability, and widespread adoption of FDTR instrumentation. We provide a detailed account of unpublished insights and institutional knowledge that are critical for obtaining accurate and repeatable measurements of thermal properties using FDTR. We discuss component selection and placement, alignment procedures, data collection parameters, common challenges, and our efforts to increase measurement automation. In FDTR, the unknown thermal properties are fit by minimizing the error between the phase lag at each frequency and the multilayer diffusive thermal model solution. For data fitting and uncertainty analysis, we compare common numerical integration methods, and we compare multiple approaches for fitting and uncertainty analysis, including Monte Carlo simulation, to demonstrate their reliability and relative speed. The instrument is validated with substrates of known thermal properties over a wide range of isotropic thermal conductivities, including Borofloat silica, quartz, sapphire, and silicon.

Published by AIP Publishing. https://doi.org/10.1063/5.0213738

https://pubs.aip.org/aip/rsi/article/95/10/103006/3316821/An-instrumentation-guide-to-measuring-thermal

Introduction to FDTR

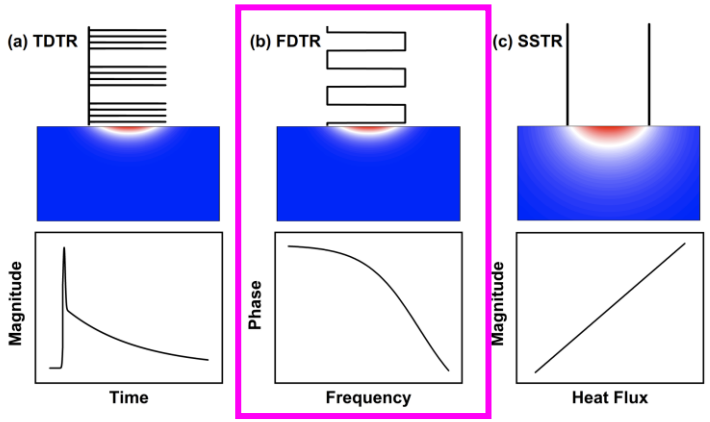

D. Olson, J. Braun, P. Hopkins, *Journal of Applied Physics* 126, 150901 (2019)

- Operates on principle of coefficient of thermoreflectance C_{TR}
- A thin transducer film is deposited on the sample
- A modulated *pump* laser (405 nm) heats the transducer, inducing a corresponding periodic change in reflectivity
- A second *probe* laser (532 nm) is coaxially focused and reflected from the surface; the reflected probe beam acquires the same modulation as the pump but with a phase lag
- The phase of the reflected *probe* beam is measured as a function of the modulation frequency of the *pump* beam (100 Hz to 20 MHz)
- Properties are obtained by modeling a fit of the phase curve
- Since the thermal penetration depth is dependent on the modulation frequency, FDTR can variably and/or simultaneously probe various depths.

Each layer is modeled using a 2D multilayer heat diffusion solved as function of frequency with a volumetric heat capacity, cross-plane and in-plane thermal conductivities, layer thickness, and thermal boundary conductance at each interface. The surface temperature is numerically solved using the heat diffusion equation.

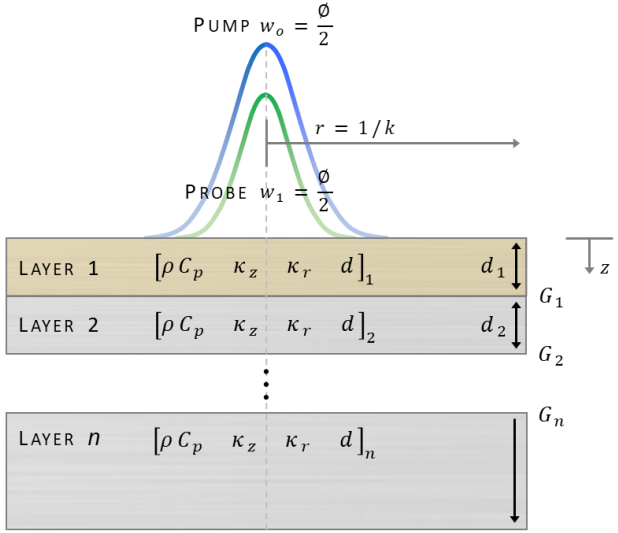

$$I(r,t) = \left(\frac{2P(t)}{\pi w_o^2}\right) e^{\frac{-2r^2}{w_o^2}}$$

ρC_p : Volumetric specific heat capacity
κ_z : Cross-plane thermal conductivity
κ_r : In-plane thermal conductivity
d_n : Layer thickness
G_n : Thermal boundary conductance

$$\mathbf{H}(r,\omega) = \frac{\kappa_r}{r}\frac{\partial}{\partial r}\left(\frac{\partial \theta}{\partial r}\right) + \kappa_z \frac{\partial^2 \theta}{\partial r^2} = \rho C_p \frac{\partial \theta}{\partial t}$$

$$\boldsymbol{H}(\omega) = \frac{A_0}{2\pi}\int_0^\infty k\left(\frac{-D}{C}\right)\exp\left(-\frac{k^2\left(w_0^2 + w_1^2\right)}{8}\right)dk$$

$$\phi = \tan^{-1}\frac{\Im\left(\mathbf{H}(r,\omega)\right)}{\Re\left(\mathbf{H}(r,\omega)\right)} + \phi_{ext}$$

D. Kirsch, J. Martin et al., Rev. Sci. Instrum. 95, 103006 (2024)

FDTR in Literature

- Initially demonstrated using both pulsed and CW lasers [1]
  - Electro-optic modulators (EOM) used to modulate pulsed or CW lasers
    - Some CW lasers can be directly digitally modulated
  - **Balanced photodetection significantly reduces measurement phase noise** [2]
  - Further studies on FDTR uncertainty calculations [3] and volumetric heating [4]
- Fiber-aligned FDTR [5]
- Broadband FDTR (200 kHz – 200 MHz) [6]
- Wide Bandwidth FDTR (0.1 Hz – 75 MHz) [7]
- Beam-offset FDTR [8]
- Deep Learning for FDTR global fitting [9]
- FDTR characterization of arbitrary geometries (Si micropillars) [10]

Challenges: FDTR instruments are generally developed in academic or government laboratories and there has yet to be heavy adoption by industry; can be difficult to construct, align, and maintain, especially for the novice. Literature primarily focuses on theory and mathematical model used for data analysis and property extraction.

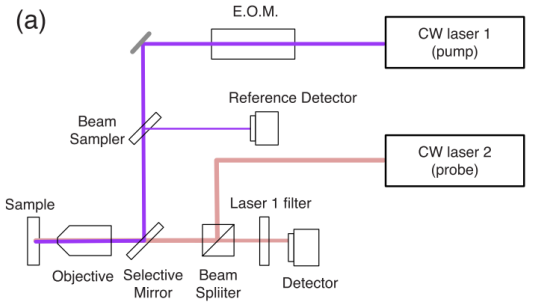

CW Laser FDTR arrangement

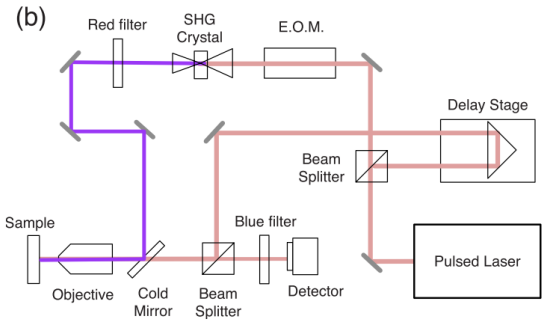

Pulsed Laser FDTR arrangement

Reference [1]

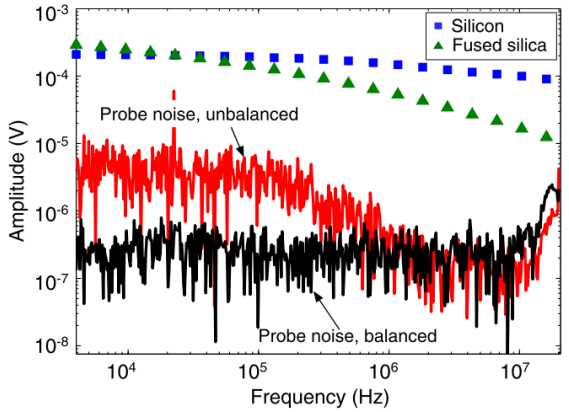

Measured FDTR signal magnitude for Si and fused silica compared to the probe noise floor for balanced and unbalanced detection. At frequencies > 10 MHz noise is dominated by coherent RF pickup in the detector and signal cables.

Reference [2]

[1] A.J. Schmidt, R. Cheaito, and M. Chiesa, Review of Scientific Instruments 80, 094901 (2009)
[2] J. Yang, C. Maragliano, and A.J. Schmidt, Review of Scientific Instruments 84, 104904 (2013)
[3] J. Yang, E. Ziade, and A.J. Schmidt, Review of Scientific Instruments 87, 014901 (2016)
[4] J. Yang, E. Ziade, and A.J. Schmidt, J Appl Phys 119, 095107 (2016)
[5] J.A. Malen et al., J Heat Transfer 133(8), 081601 (2011).
[6] K.T. Regner, S. Majumdar, and J.A. Malen, Review of Scientific Instruments 84, 064901 (2013).
[7] E. Ziade, Review of Scientific Instruments 91, 124901 (2020)
[8] M. Rahman et al., J Appl Phys 123, 245110 (2018)
[9] W. Shen, D. Vaca, and S. Kumar, Nanoscale and Microscale Thermophysical Engineering 24(3–4), 138–149 (2020)
[10] R.J. Warzoha, et al., J Appl Phys 129, 035103 (2021)

NIST Custom FDTR Instrument

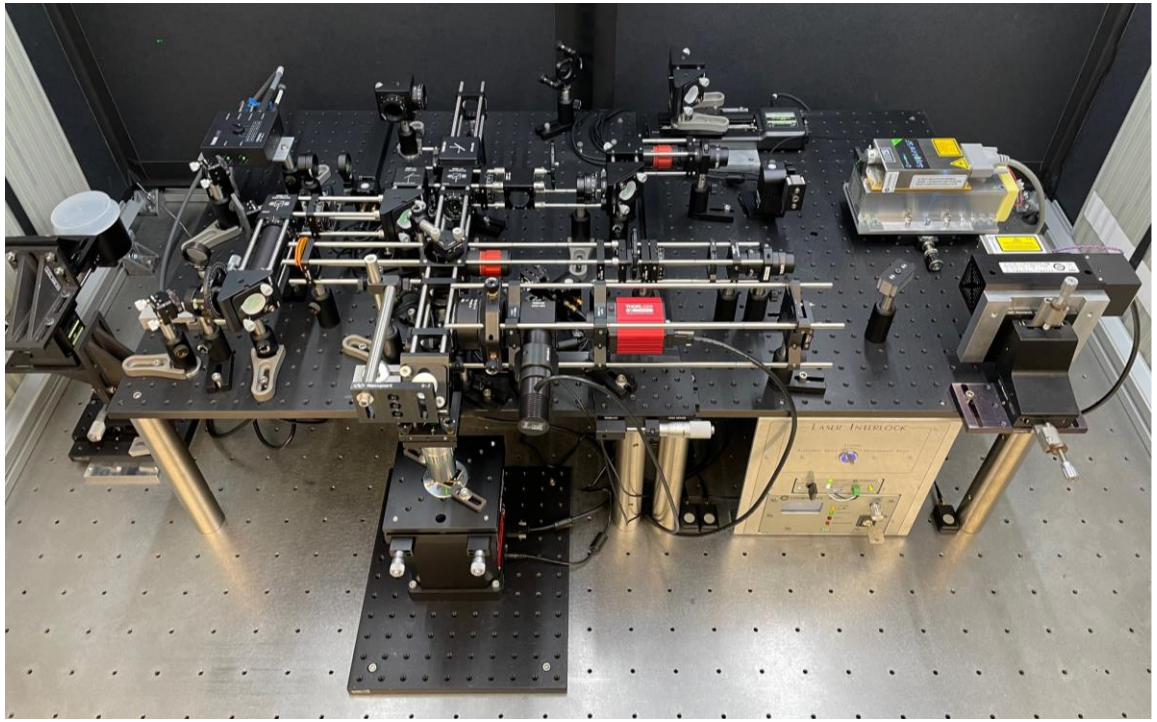

Current optical table layout of the NIST FDTR Instrument

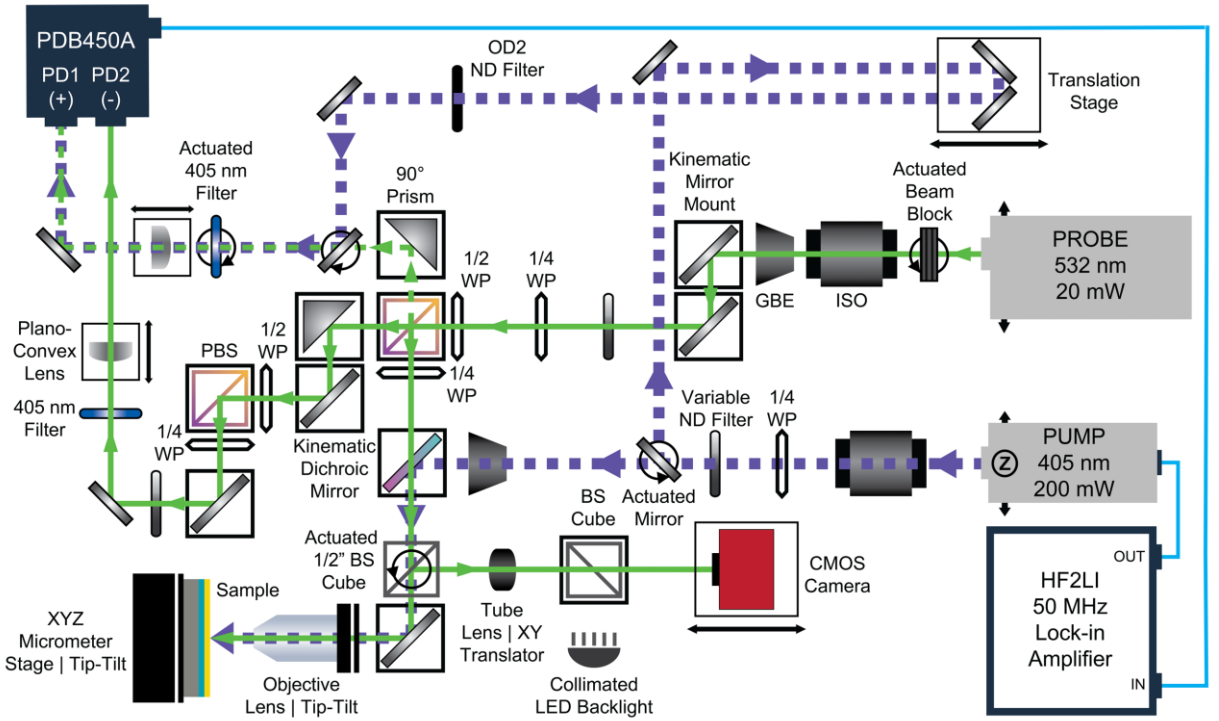

Combined beam path diagram

- Probe Laser - Continuous wave (CW) Coherent Sapphire SF 532 nm 20 mW; excellent spatial qualities ($M^2 \leq 1.1$) and Au C_{TR} peak
- Pump Laser - CW Coherent OBIS LX 405 can be digitally modulated up 150 MHz good beam quality ($M^2 \leq 1.3$), 405 nm has absorbance of 60 %
- **Thorlabs PDB450A Adjustable Gain Balanced (PDB) amplified photodiode (set to 45 MHz setting)**
- **Zurich Instruments HF2LI 50 MHz Lock-in amplifier (LIA) and signal generator**
- **Compact 30 mm cage setup for modularity and long-term stability**

- **Custom interlocked light-tight optical enclosure constructed from Bosch 45mm Aluminum framing**
- **Actuated (motorized) 90° optical component flippers**
  - Automated and repeatable switching between beam path "modes"
  - Measurement, pump reference, pump leak, and camera mode
- **CMOS Camera for sample imaging and (probe beam focal plane imaging)**
- **Motorized XYZ sample stage and motorized pump reference delay stage**

D. Kirsch, J. Martin et al., Rev. Sci. Instrum. 95, 103006 (2024)

Instrument Automation – LabVIEW

- **Custom LabVIEW control software and interface created with Dr. Joshua Martin's expertise**
  - Unique User Interface created for touchscreen monitor instrument control
- **The entire measurement is automated using the custom LabVIEW code**
  - Optical component flippers (measurement, leak, reference, and camera modes)
  - XYZ motorized stages
  - Pump and probe laser operation
  - LIA data acquisition & pump modulation signal generation
  - Real time data visualizations from the LIA
  - Optical enclosure laser safety interlock monitoring
- **Accommodates 76.2 mm DIA thin films, multilayer systems, or bulk samples (@ RT); automated property maps can be obtained using the XY scanning platform**

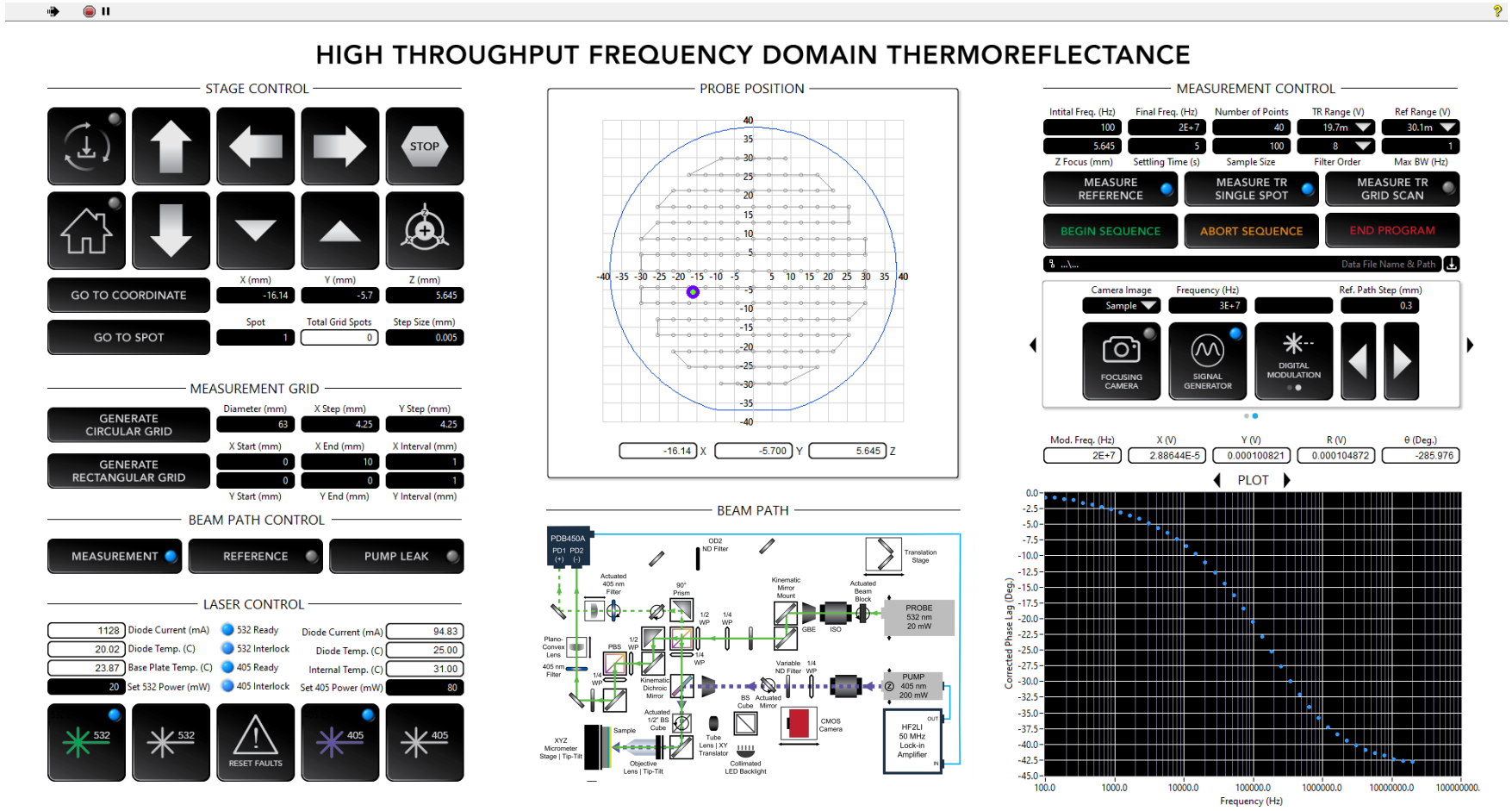

D. Kirsch, J. Martin et al., Rev. Sci. Instrum. 95, 103006 (2024)

Measurement Mode and Pump Digital Modulation

- Use dichroic mirror to coaxially align pump with probe beam
- Use PBS to split probe into (low power) sample and reference paths
- Use $\frac{\lambda}{2}$ waveplate to set probe incident power (≈ 1 mW to ≈ 2 mW) and post-sample reflected probe beam intensity on PD+
- Adjust $\frac{\lambda}{4}$ to obtain maximum post-sample probe transmission through PBS
- DC magnitude of post-sample and reference probe beams must be equaled before a measurement (ND filter on probe reference)
    - Connect PD+ and PD- fast outputs of the PDB to the LIA AUX inputs

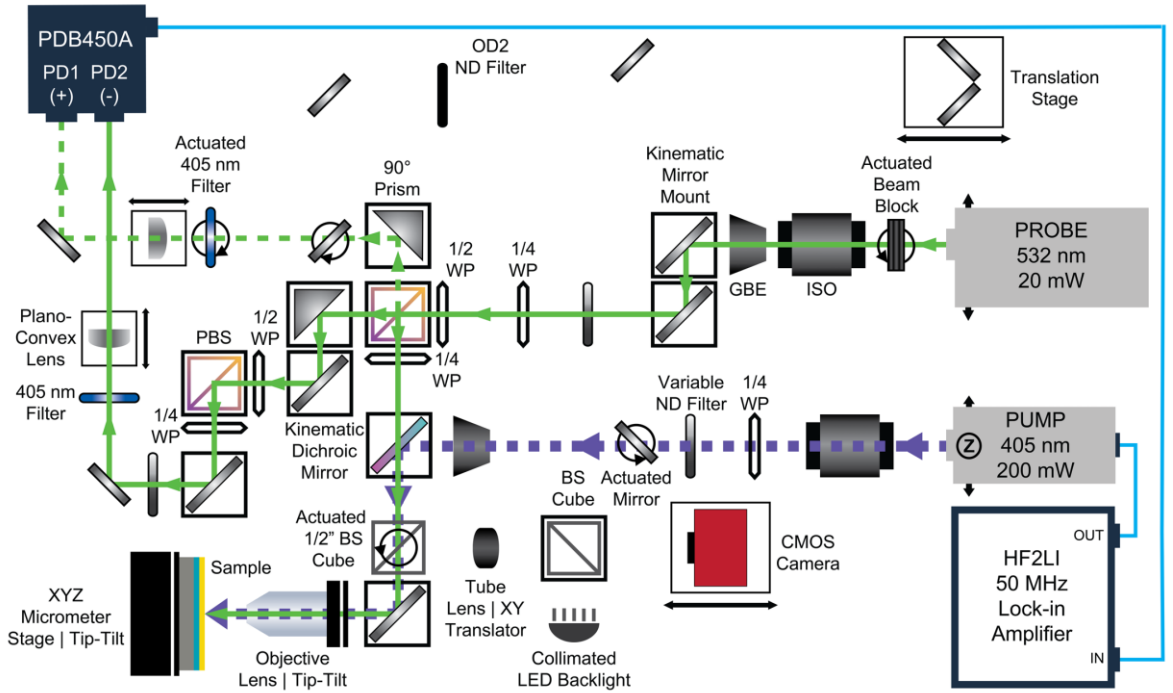

Measurement Mode beam path diagram

Representative pump modulation waveforms at select frequencies (measured using the BPD RF output in Reference Mode while connected to a Tektronix TDS2002B Oscilloscope).

- The HF2LI output total harmonic distortion increases above 1 MHz and may influence the waveform (Figure 9.12 in the HF2LI User Manual).

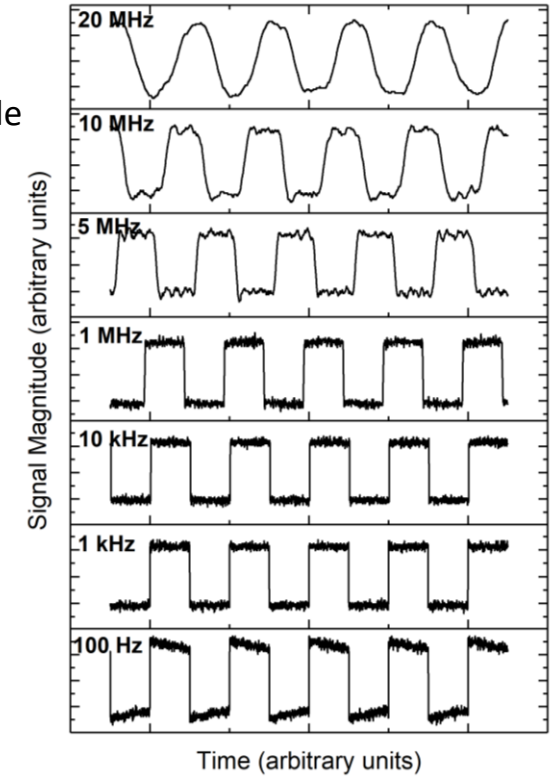

Typical HF2LI settings for the sweeper module and OBIS pump laser modulation.

Commands	Value	Unit
sigouts/0/range	10	V
sigouts/0/amplitudes/6	0.25 [a]	—
sigouts/0/offset	0.25 [a]	—
sigins/0/ac	0 (Off)	—
sigins/0/imp50	1 (On)	—
sigins/0/diff	0 (Off)	—
demods/0/order	8	—
demods/0/timeconstant	0.04788	s
demods/0/rate	1779	Sa/s

[a] Note: The command value is not in units of V (as displayed in LabOne); this value is a factor that is multiplied by the range.

D. Kirsch, J. Martin et al., Rev. Sci. Instrum. 95, 103006 (2024)

Leak Mode

- $\phi(\omega)_{system}$ includes contributions from the cables, the photodiode and amplifier circuits, other electronic components, ***and the modulated post-sample pump beam that leaks through the bandpass filter***
- Probe beam is blocked and bandpass filter lowered to allow reflected post-sample pump beam that leaks through the dichroic mirror to be incident on the PD+ signal photodiode (***after finding probe focal plane***)
  - Use same PD+ TR signal diode
- Pump beam modulated at 30 MHz for leak measurement
  - Frequency above the highest value in measurement sweep (large enough for changes in the path length to finely tune the change in phase) but below the maximum value of the photodetector bandwidth
- Leak phase time averaged using the LIA plotter function
- **Improperly focused beam can perturb the measured phase, verify on setup that the PD+ voltage from the pump leak beam and the post-sample probe beam are both maximized by adjusting the PD+ kinematic mirror**

$$\phi(\omega)_{LI} = \phi(\omega) + \phi(\omega)_{system}$$

$\phi(\omega)_{LI}$ → Measured phase on the LIA

$\phi(\omega)$ → Phase lag from the sample

$\phi(\omega)_{system}$ → External system phase

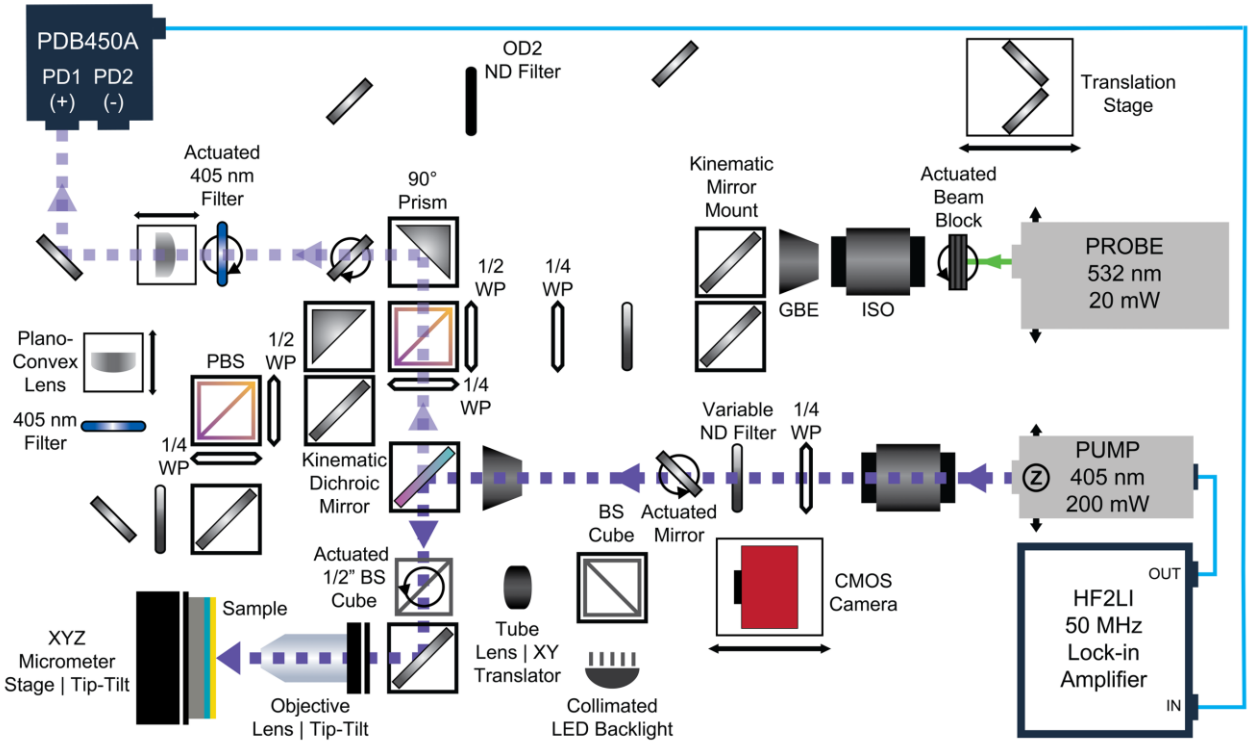

Leak Mode beam path diagram

D. Kirsch, J. Martin et al., Rev. Sci. Instrum. 95, 103006 (2024)

Reference Mode

- **$\phi(\omega)_{system}$ measured using a separate pump reference path phase matched with the phase of the post-sample pump leak** and with a lower uncertainty than measuring the system phase directly using the post-sample pump beam
  - The laser power directed through the pump reference path is 10 to 20 times larger than the post-sample leak pump beam transmitted through the dichroic, the signal magnitude is larger and adjustable with a corresponding smaller phase noise
- Pump beam directed into reference path and through delay stage using an actuated flipper mirror
- **Pump reference path length adjusted to phase match the pump leak value to within ± 0.1 ° at 30 MHz**
- $\phi(\omega)_{system}$ measured over the same range and interval as the sample measurement (100 Hz to 20 MHz)
- **The reference phase measured at each frequency is subtracted from the post-sample probe phase measurements to obtain the corrected phase**

$$\phi(\omega)_{LI} = \phi(\omega) + \phi(\omega)_{system}$$

$\phi(\omega)_{LI}$ → Measured phase on the LIA

$\phi(\omega)$ → Phase lag from the sample

$\phi(\omega)_{system}$ → External system phase

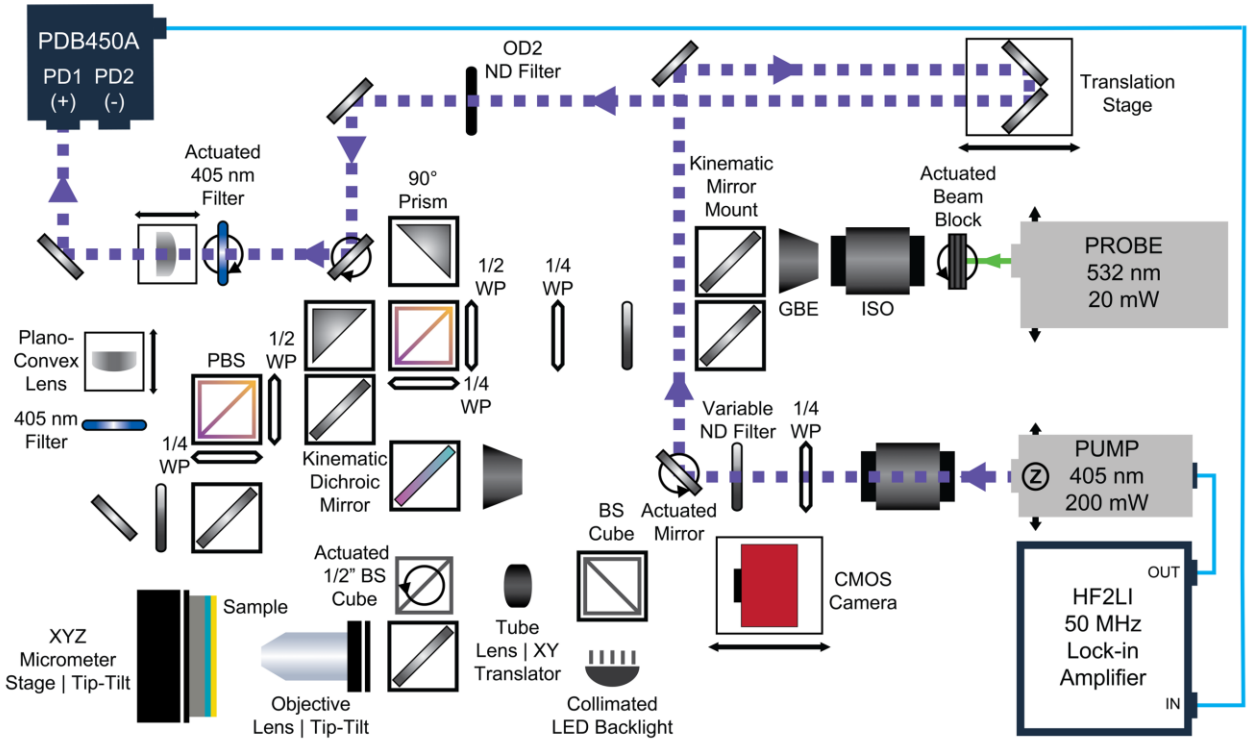

D. Kirsch, J. Martin et al., Rev. Sci. Instrum. 95, 103006 (2024)

Phase Sensitivity Calculations

- **The ability to simultaneously measure a selected set of parameters is visualized by calculating the phase sensitivity $S_x(\omega)$ (in degrees)**
  - Shows which parameters can be extracted with the highest confidence, the frequency region in which those parameters are the most sensitive, and for simultaneously extracted unknown parameters, if the sensitivity peaks overlap
- **Calculated as the phase response to a small (1 %) perturbation of a selected thermal parameter, x, (κ, G, C_V, w_0, and/or w_1)**
- **$S_x(\omega)$ shown for reference substrates: Borofloat silica glass, quartz, sapphire, and silicon (Si)**
- **Pump radius** (w_0, black curve) **has the largest sensitivity** across the frequency space and for all materials considered in this work
- Sensitive to the transducer volumetric heat capacity (C_V^{Au}, blue curve) and the transducer thickness (d^{Au}, orange curve), but ***insensitive to the transducer thermal conductivity*** (κ_{iso}^{Au}, purple curve) for all frequencies and for these substrates
- **General Rule of Thumb - Model is most sensitive to the largest thermal resistor (or capacitor, if fitting for the volumetric heat capacity)**

$$\phi = \tan^{-1}\frac{\Im\left(\mathbf{H}(r,\omega)\right)}{\Re\left(\mathbf{H}(r,\omega)\right)} + \phi_{ext}$$

$$S_x(\omega) = \frac{\partial\phi(\omega)}{\partial \ln x}$$

Substrate	XRR Au+Ti Transducer Thickness d (nm)	Au+Ti Transducer Reference Property Values ρC_p (MJ m^{-3} K^{-1})	Au+Ti Transducer Reference Property Values κ_{iso} (W m^{-1} K^{-1})	Substrate Reference Property Values ρC_p (MJ m^{-3} K^{-1})	Substrate Reference Property Values κ_{iso} (W m^{-1} K^{-1})
Borofloat Silica Glass	80	2.48 ± 0.07	220 ± 10	1.83 ± 0.1	1.41 ± 0.07
Quartz	75			2.0 ± 0.2	8.15 ± 1.0
Sapphire	78			3.06 ± 0.1	35.0 ± 5
Silicon	75			1.66 ± 0.1	145 ± 10

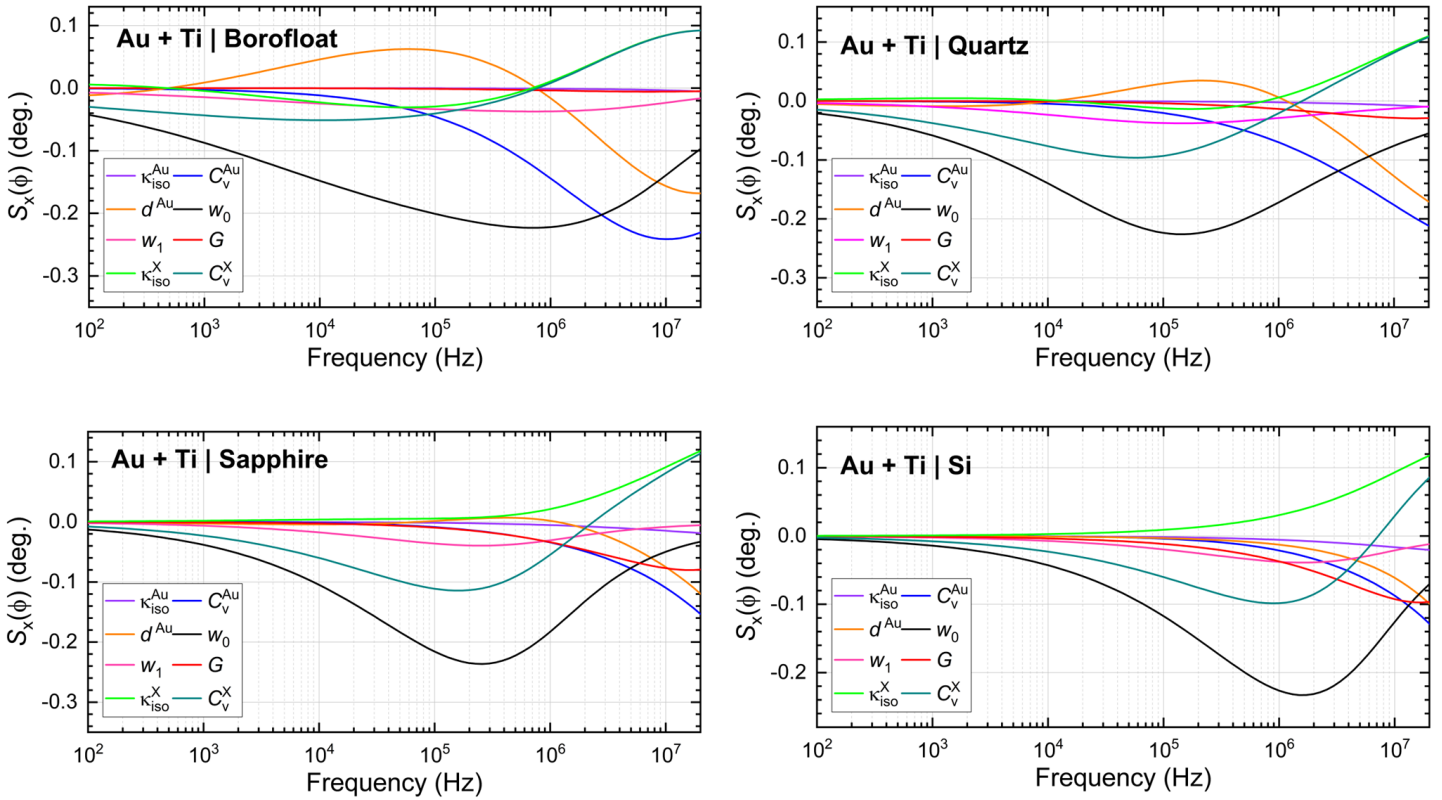

D. Kirsch, J. Martin et al., Rev. Sci. Instrum. 95, 103006 (2024)

Transducer Deposition

- **Reproducible deposition of high-quality transducer films is critical, since the transducer thickness, thermal conductivity, and heat capacity are model input parameters**
  - The transducer surface roughness, adhesion, the interface conductance, and density may also affect the measured phase
- **2 nm to 5 nm thick adhesion layer of Ti or Cr enhances mechanical robustness of Au transducer and thermal interface conductance**
- Sputtering or electron beam evaporation typically used to deposit transducers
- Limited research on the influence of transducer deposition methods on TR measurements; the study by [1] did not find a significant difference between the sputtering and electron-beam evaporation methods
- NIST NanoFab 4wave Ion-Beam Deposition/Biased-Target Deposition (IBD/BTD) Cluster Sputter Instrument used for transducer and adhesion layer deposition
  - BTD is a hybrid technique of IBD and conventional sputter deposition
    - Low energy ion beam sputters material from a large diameter negatively biased target; a second ion beam aimed at the surface of the substrate
    - ***Produces high quality, uniform, pinhole free, fully dense films***
  - 13” automated sample cassette enables uniform coating on many samples at once
  - Cryo pumped to 2.6 x 10^{-6} Pa (2 x 10^{-8} Torr)
  - Crucial to reduce oxygen contamination of the Ti interface layer [2][3]
  - Planning to do a transducer deposition method and thickness study

NIST NanoFab 4wave IBD/BTD deposition instrument

[1] E. Ziade, Review of Scientific Instruments 91, 124901 (2020)

[2] D.H. Olson, K.M. Freedy, S.J. McDonnell, and P.E. Hopkins, Appl Phys Lett 112, 171602 (2018).

[3] D.H. Olson et al., Appl Phys Lett 118, 163503 (2021)

Transducer Thickness

- Schmidt et al. found **little dependence of FDTR measured thermal conductivity as a function of Au transducer thicknesses > 50 nm** (using a pulsed 400 nm pump and a 815 nm probe laser). [1]
- **We deposit films with a nominal thickness of ≈ 80 nm Au and a ≈ 2 nm Ti adhesion layer** to ensure thermalization of the irradiated electrons[2] (based on transducer thickness used in similar FDTR instrumentation [3],[4] and discussions with community)
- We are actively investigating how the transducer thicknesses, the adhesion layer element, the vacuum level, and the deposition method influence the extracted thermal properties for the time regimes used in more typical FDTR measurements.

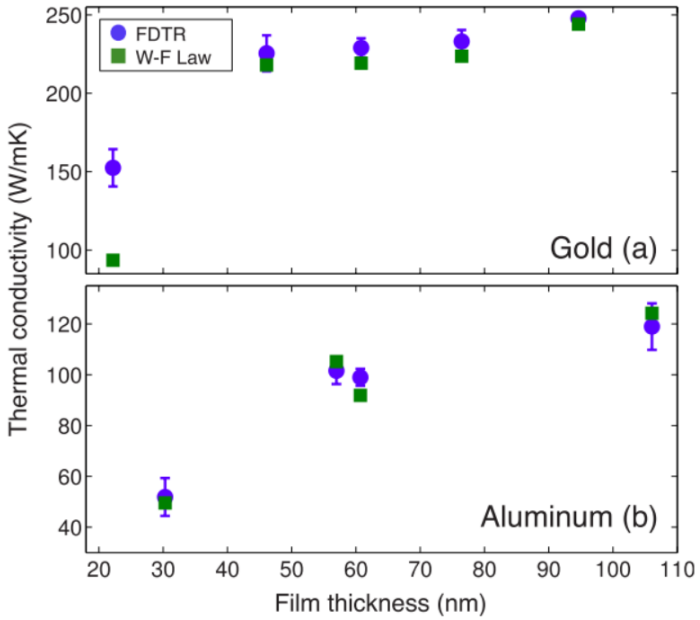

FIG. 4. (Color online) Thermal conductivity data obtained for (a) Au and (b) Al films on fused silica substrates. Circles are values obtained with the FDTR method, while the squares are values computed from electrical conductivity measurements using the WF law.

Reference [1]

[1]. A.J. Schmidt, R. Cheaito, and M. Chiesa, Appl Phys 107, 024908 (2010).
[2] R.B. Wilson, J.P. Feser, G.T. Hohensee, and D.G. Cahill, Phys Rev B 88, 144305 (2013)
[3] J. Yang, E. Ziade, and A.J. Schmidt, Review of Scientific Instruments 87, 014901 (2016)
[4] B.F. Donovan, R.J. Warzoha et al., Macromolecules 53(24), 11089–11097 (2020)

Transducer Characterization

- Contact profilometry or X-Ray Reflectometry (XRR) to measure transducer thickness
- **X-Ray Reflectometry (XRR) is especially useful used for characterizing the thickness, roughness, and density of thin films** (best for thicknesses between 2 nm to 200 nm)
- NIST Rigaku Smartlab X-ray diffractometer
  - $2\theta = 0\,^\circ$ to $2\theta = 6\,^\circ$, every $0.004\,^\circ$ step → 1500 pairs of intensity and 2θ data
  - Fit against a stack electron density model which simulates the specular reflections and refractions from each film layer, as well as the roughness profiles encountered at each interface
  - ***Thickness is averaged over the scan area (≈ 10 mm wide for our measurements)***
- XRR fitted using a custom differential evolution (genetic algorithm) parameter optimization approach and followed by a series of coupled Markov Chain Monte Carlo (MCMC) simulations (using REFL1D open-source software package)
- Misalignment, X-ray energy, and surface and interface roughness uncertainties are combined using the NIST Uncertainty Machine (https://uncertainty.nist.gov/)
- The Au thickness and uncertainty determined with and without inclusion of a Ti adhesion layer are compared using the NIST Consensus Builder by using both Linear Pool and Hierarchical Bayes methods (and keeping whichever is larger) to produce an overall uncertainty budget.
- XRR measurement and uncertainty analysis by Dr. Donald Windover (NIST)

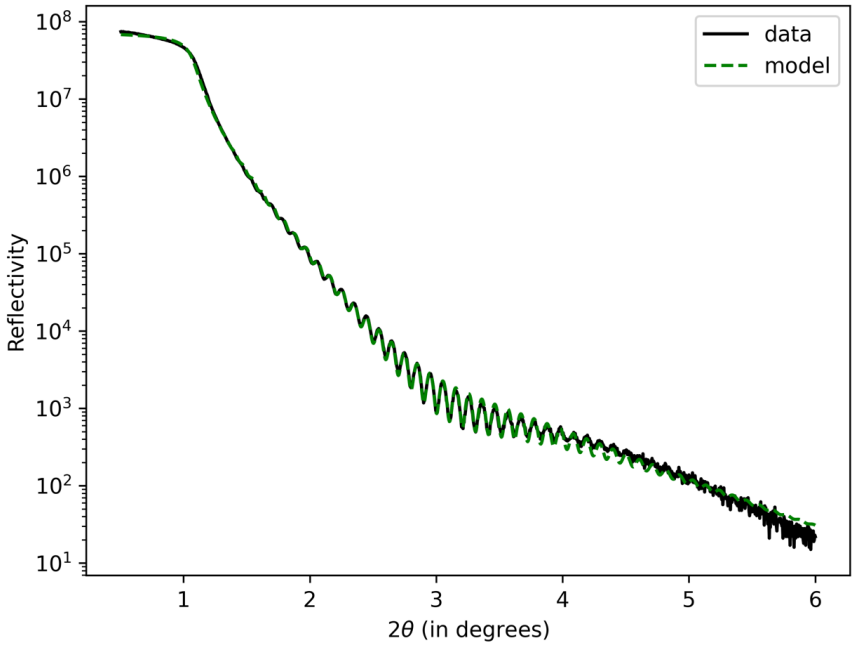

Representative XRR data and model fit for a Au+Ti | Si witness chip. Transducer layer thickness is 78.1 ± 0.44 nm (1 sigma).

[1] https://uncertainty.nist.gov/

D. Kirsch, J. Martin et al., Rev. Sci. Instrum. 95, 103006 (2024)

Laser Spot Size Characterization

- **Knife-edge** measurements are the common way laser beam sizes are characterized
  - **Automated version available commercially**
  - Limited to beam diameters > 2.5 µm
- **Thorlabs BP209VIS Knife Edge Beam Profiler (1) on a custom mount with motorized z-stage (2)**
  - **Precisely place profiler at the objective at the focal plane & find minimum probe size**
  - **Pump diameter measured at same z**
  - Measured at both +45 ° and -45 °
- **Manual XY micrometers (3) enable the beam to be centered on the profiler sensor**
- Advantageous to mount on a tip/tilt to avoid an incident angle
- Galilean Beam Expanders enable adjustment of the beam sizes at the focal plane
- Probe DIA = 5.5 µm; Pump DIA = 13.5 µm
- Probe diameter uncertainty ± 0.1 µm (1*u*); Pump diameter uncertainty ± 0.2 µm (1*u*)

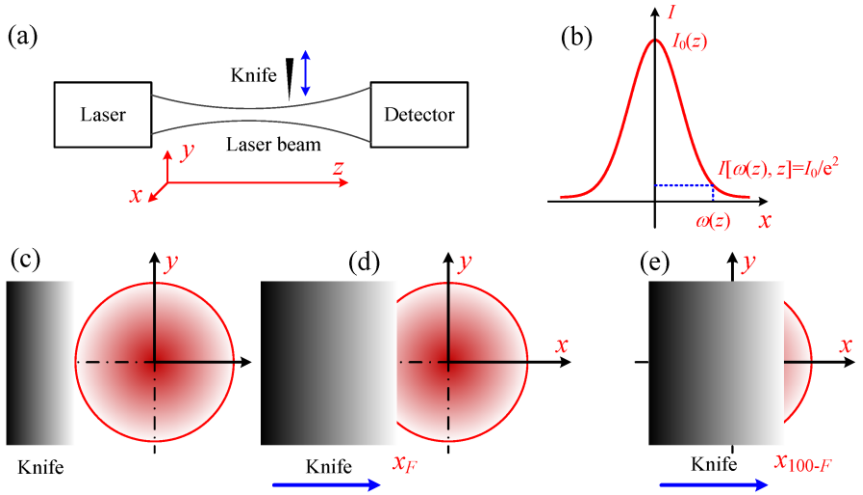

Chen et al., Nanomaterials 2017, 7(12), 416

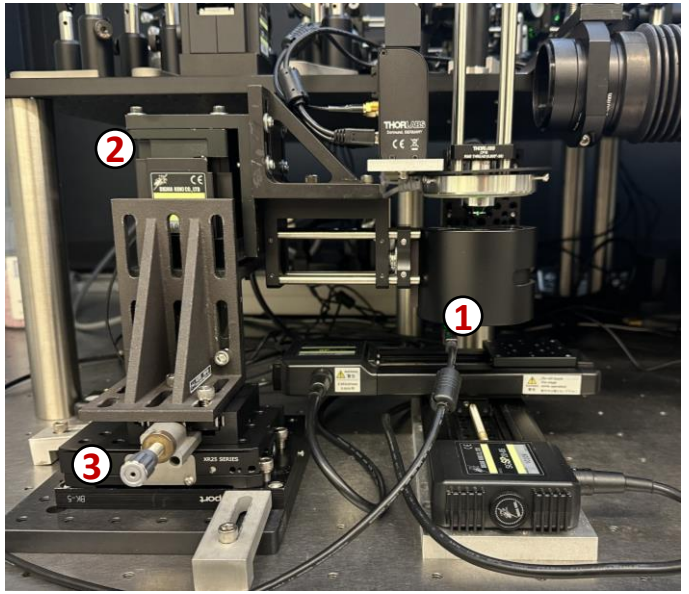

https://www.thorlabs.com/newgrouppage9.cfm?objectgroup_id=804

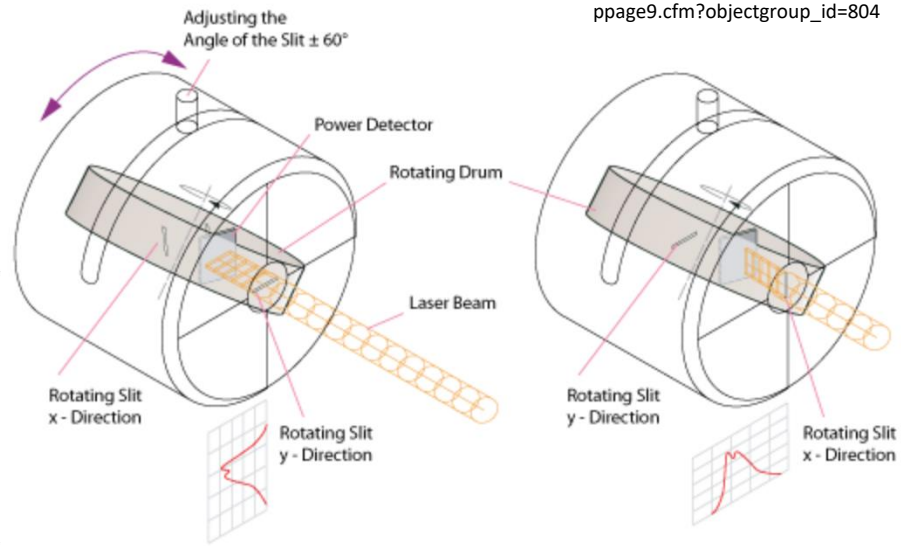

Laser Spot Size Characterization – Profiler Settings

- Knife edge mode
- Keep laser output power constant and adjust incident power with ND filters
  - **Target image saturation ≈ 80 %**
- **Gain of 4 works best for our wavelengths and spot sizes**, can be adjusted if needed (Different than Thorlabs recommended settings of automatic Gain mode)
- **Ability to record 1/e² beam diameter data over time to obtain an average and standard deviation**

https://www.thorlabs.com/newgroupppage9.cfm?objectgroup_id=804

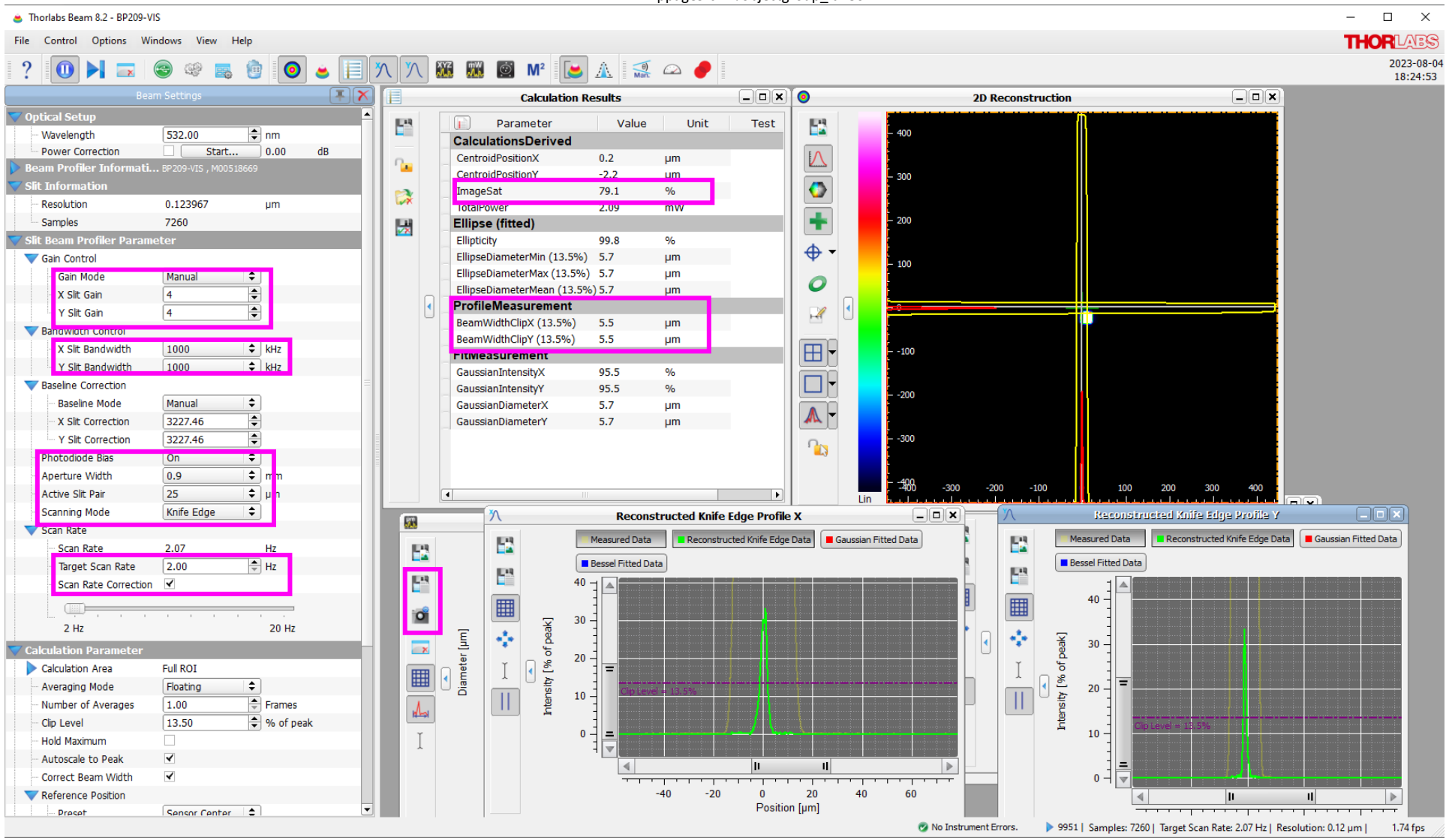

Sample Focusing & Camera Alignment

The sample surface must be positioned at the objective focal plane to reproduce the spot sizes measured by the profiler

- **Common approach: maximize the post-sample probe PD+ photodiode DC voltage**
  - DC voltage can be dependent on the focal length and position of the lens
  - There may not be a clear voltage peak (focal depth of objective)
- **A complementary approach: utilize a camera system to image both the probe beam and the sample surface**
- Higher magnification (20X) with smaller focal depth can facilitate easier setup
- If camera exposure and probe beam power are sufficiently reduced to avoid oversaturating the camera, simultaneous minimization of the central spot and the array of spots may be observed
- **Z height is adjusted until the diffraction pattern spots are minimized and uniform**
- **Once the camera system is properly setup, imaging either the probe or the sample surface, or a combination can be used to place the sample in the focal plane.**

Original imaging setup using actuated pellicle and ring light

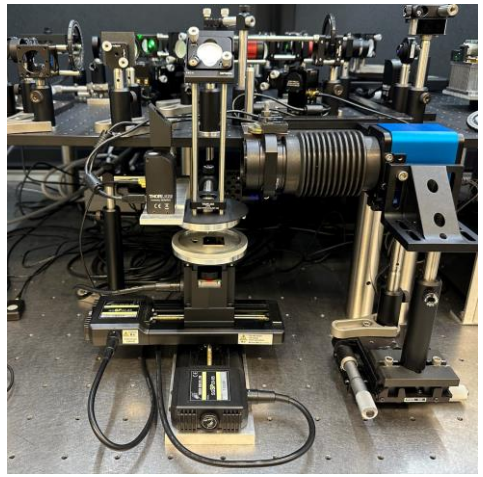

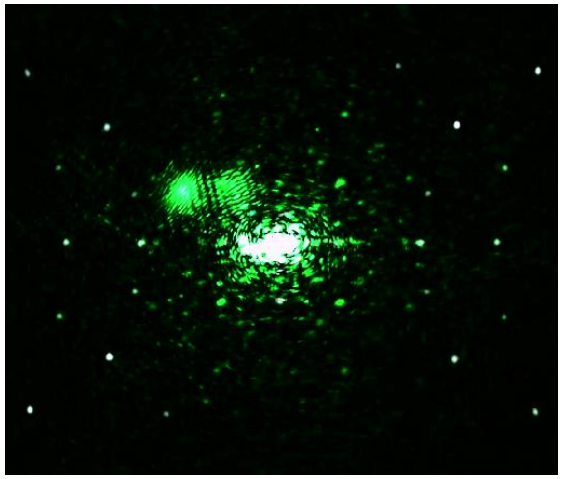

Focused probe beam on the CMOS camera

Ring light image of the Au transducer sample surface

Upgraded imaging setup using actuated beam splitter cube and collimated LED backlight

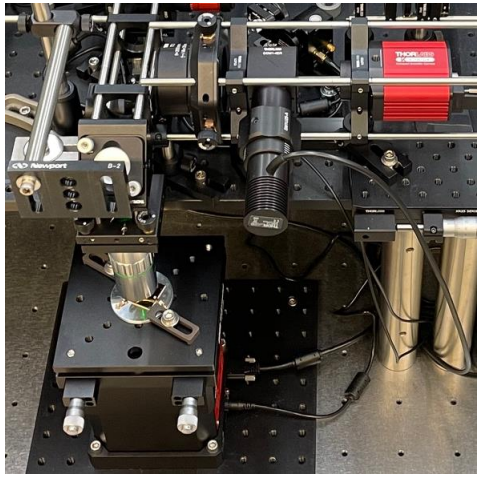

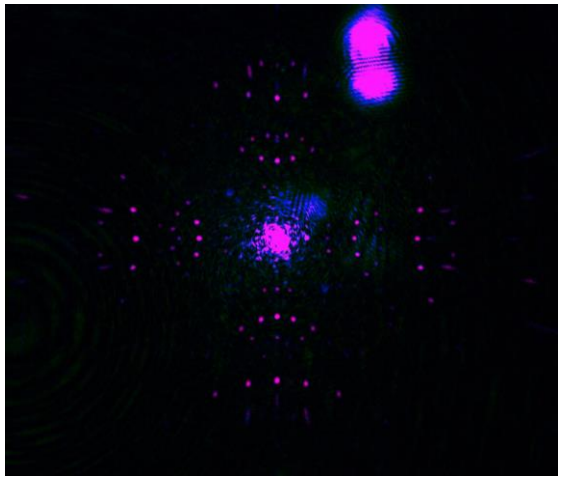

Focused probe beam on the CMOS camera

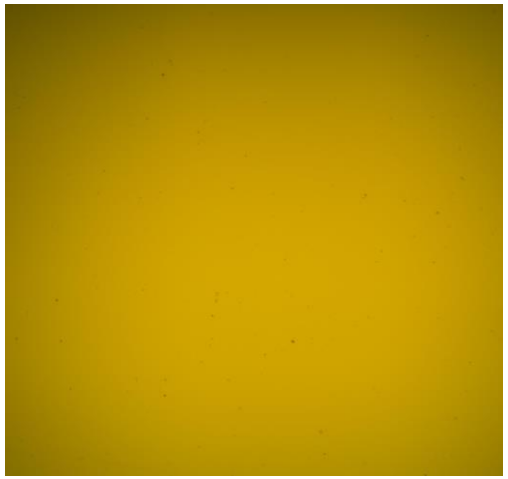

Backlight image of the Au transducer sample surface

D. Kirsch, J. Martin et al., Rev. Sci. Instrum. 95, 103006 (2024)

Laser Diffraction Patterns Reports in Literature

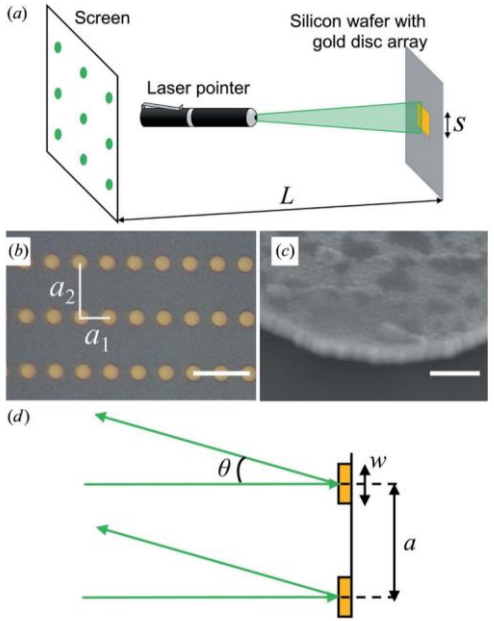

Figure 1
(*a*) Experimental setup to demonstrate the reciprocal space with laser diffraction from an Au microdisc array. (*b*) Microscopy image of an Au microdisc array (scale bar 10 μm). (*c*) Higher-magnification SEM image, tilt 30°, showing the edge of a single microdisc (scale bar 300 nm). (*d*) Schematic of the diffraction geometry.

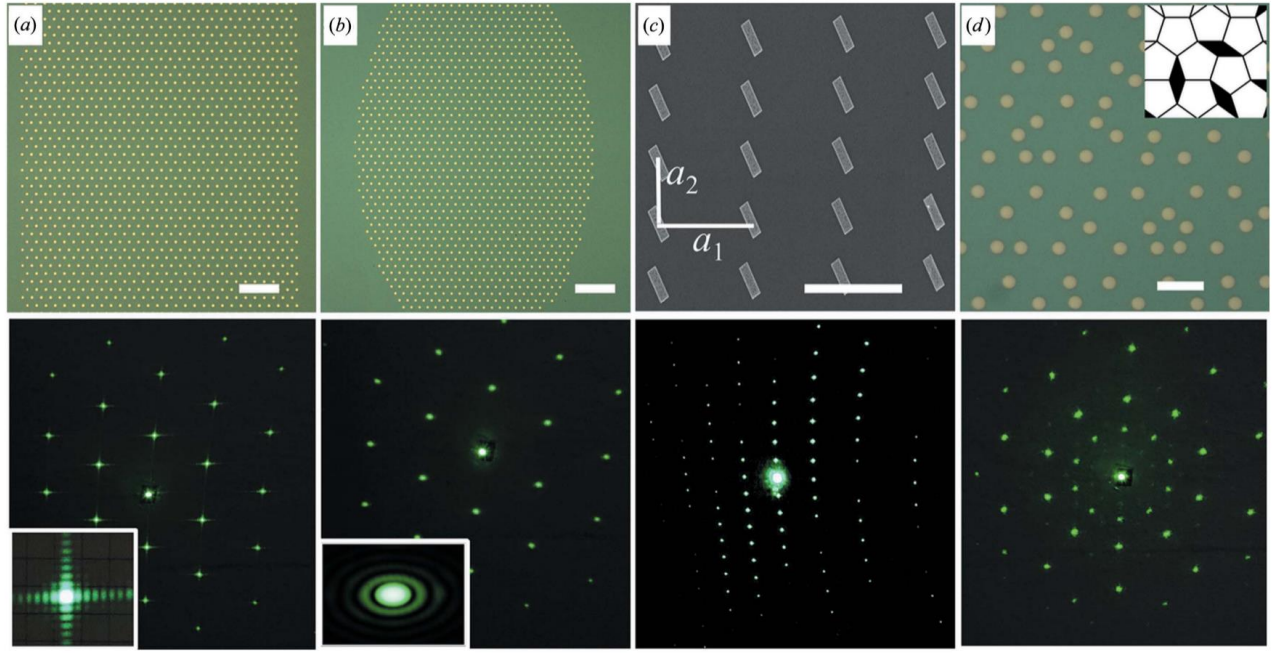

Figure 3
(*a*) Rectangular-shaped array with a hexagonal lattice (scale bar 50 μm). (*b*) Elliptical-shaped array with a hexagonal lattice (scale bar 50 μm). (*c*) SEM showing an array of tilted rectangles (scale bar 10 μm). (*d*) Quasicrystal pattern (scale bar 10 μm). In (*a*)–(*d*) the corresponding diffraction patterns are shown below. The insets in (*a*) and (*b*) show high-resolution photographs of the individual Bragg peaks.

L. Chayanun, J. Gustafson, and J. Wallentin, J Appl Crystallogr 55, 168–171 (2022).

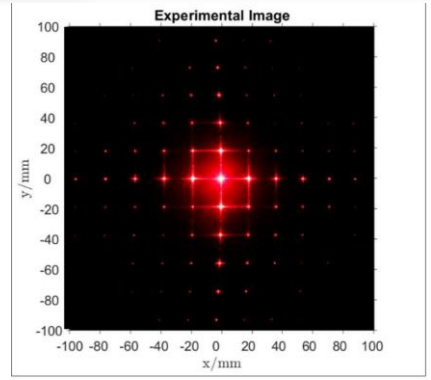

Figure 15. Experimental image taken in the laboratory, for a Melles Griot Helium-Neon Laser, with a wavelength of 632.8 nm, falling in a DMD array of square micromirrors in the FLAT state, with 13 μm in size and with a spatial frequency of 13.6 μm, projected onto a target at a focal distance of 400 mm.

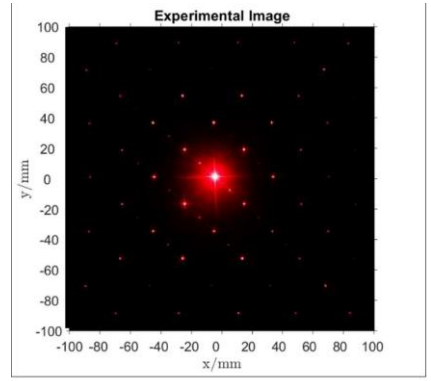

Figure 19. Experimental image taken in the laboratory, for a Melles Griot Helium-Neon Laser, with a wavelength of 632.8 nm, falling in a DMD array of micromirrors rotated 12°, with 13 μm in size and with a spatial frequency of 13.6 μm, projected onto a target at a focal distance of 400 mm.

Additional report:
K. Sun, L. Huang, X. Cheng, and H. Jiang, "Analysis and simulation of the phenomenon of secondary spots of the TDI CCD camera irradiated by CW laser," Opt Express 19, 23901–23907 (2011).

C. Pereira, M. Abreu, A. Cabral, and J.M. Rebordão, J Phys Conf Ser 2407, 012048 (2022).

Camera Alignment and Sample Focusing – Procedure

Step 1: With the probe incident, move the sample Z-height up until the diffraction spots are in focus on the camera

(Fix the Tube Lens within the stated pupil distance. On a newly setup system, a good starting point for this process is when the back reflected probe on the detector lens is at a minimum size)

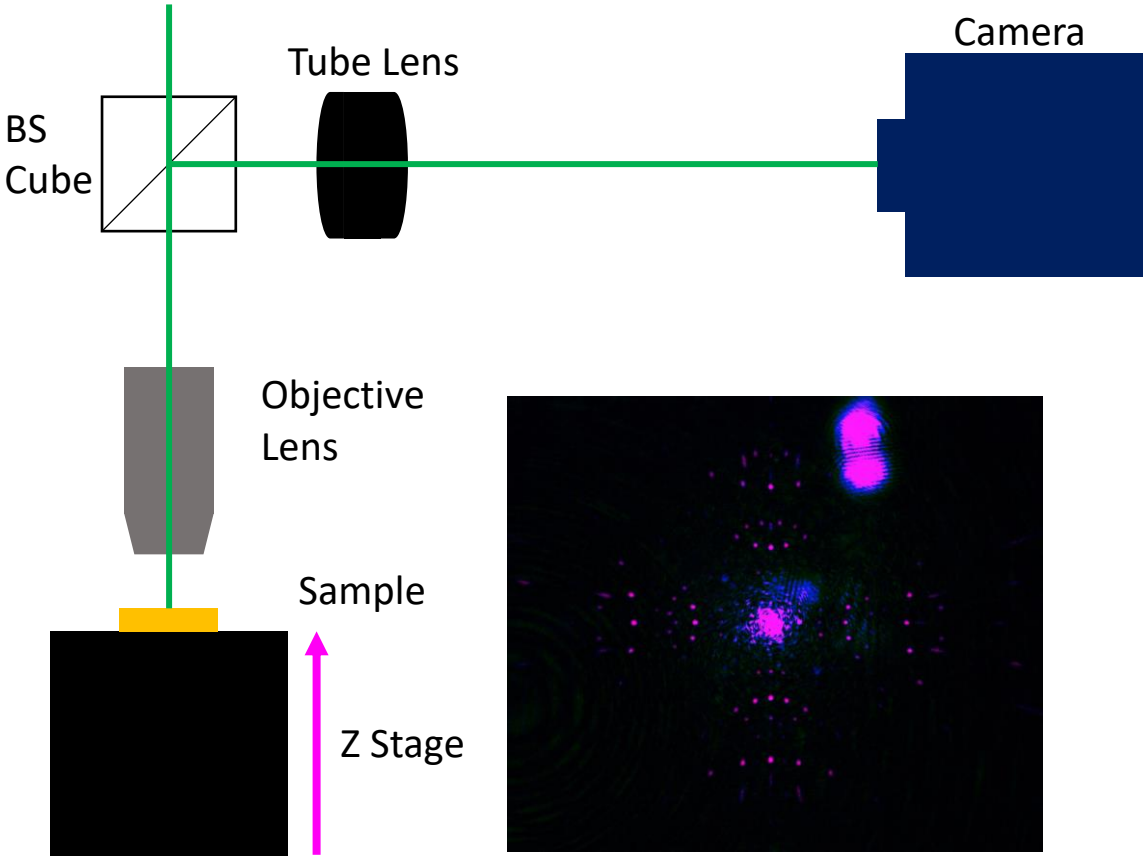

Step 2: Switch to imaging the sample surface and translate the camera until the dust on the surface is in focus.

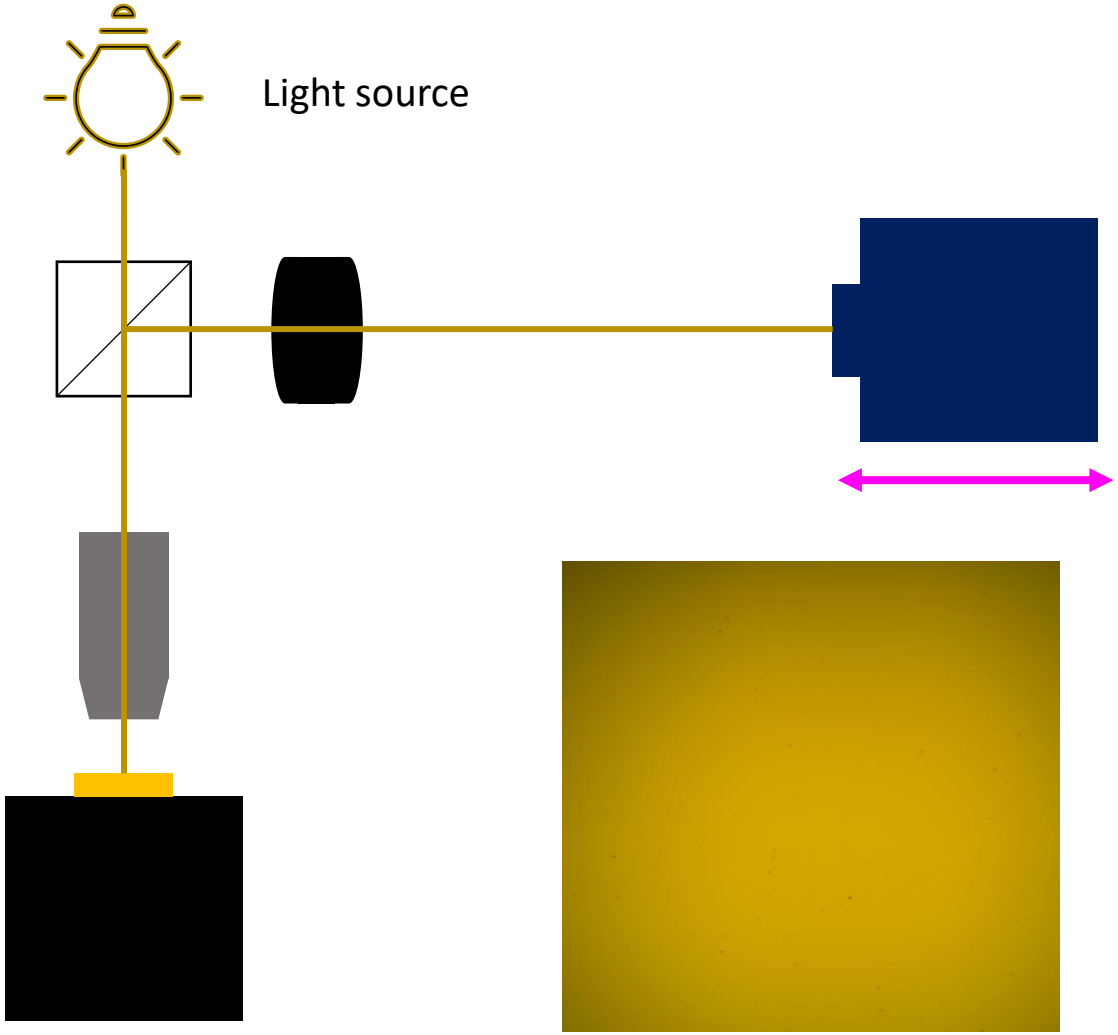

Camera Alignment and Sample Focusing – Procedure

Step 3: Now iterate - return to imaging the probe and move the Z-height of the sample until the probe diffraction spots are in focus.

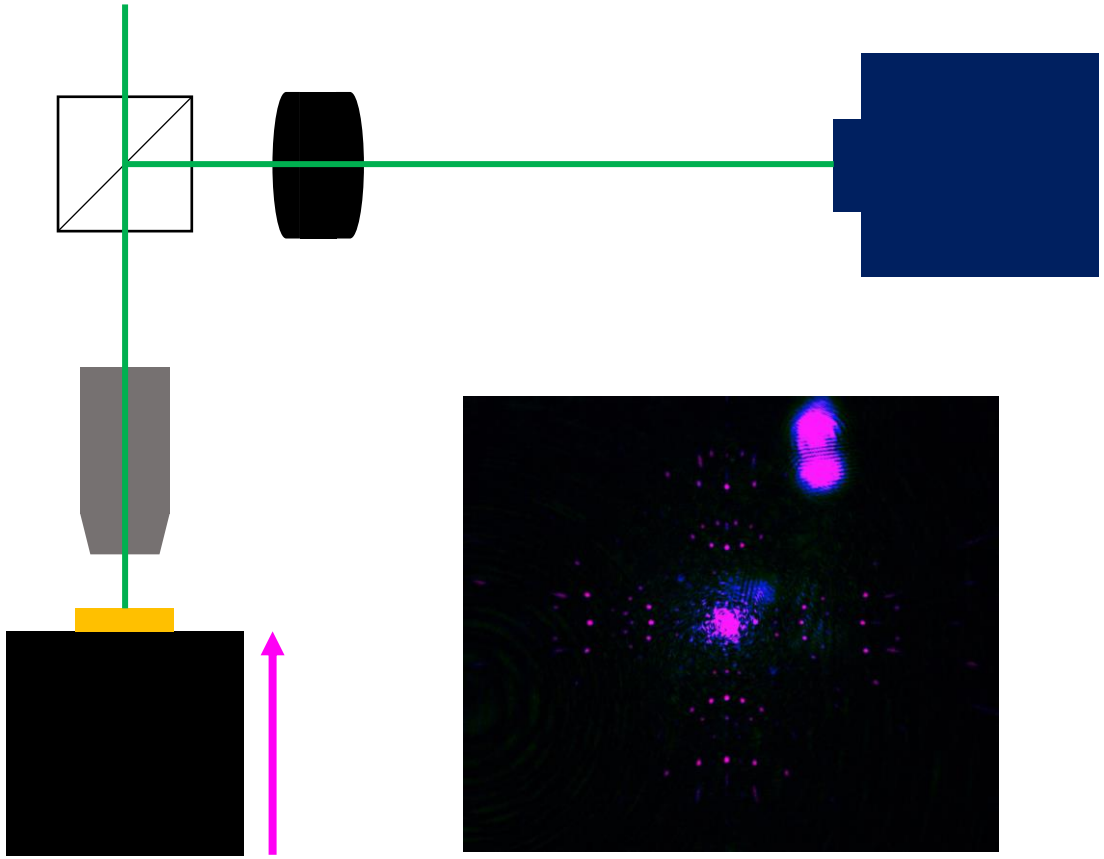

Step 4: Switch back to the surface, and again translate the camera until the dust on the surface is in focus.

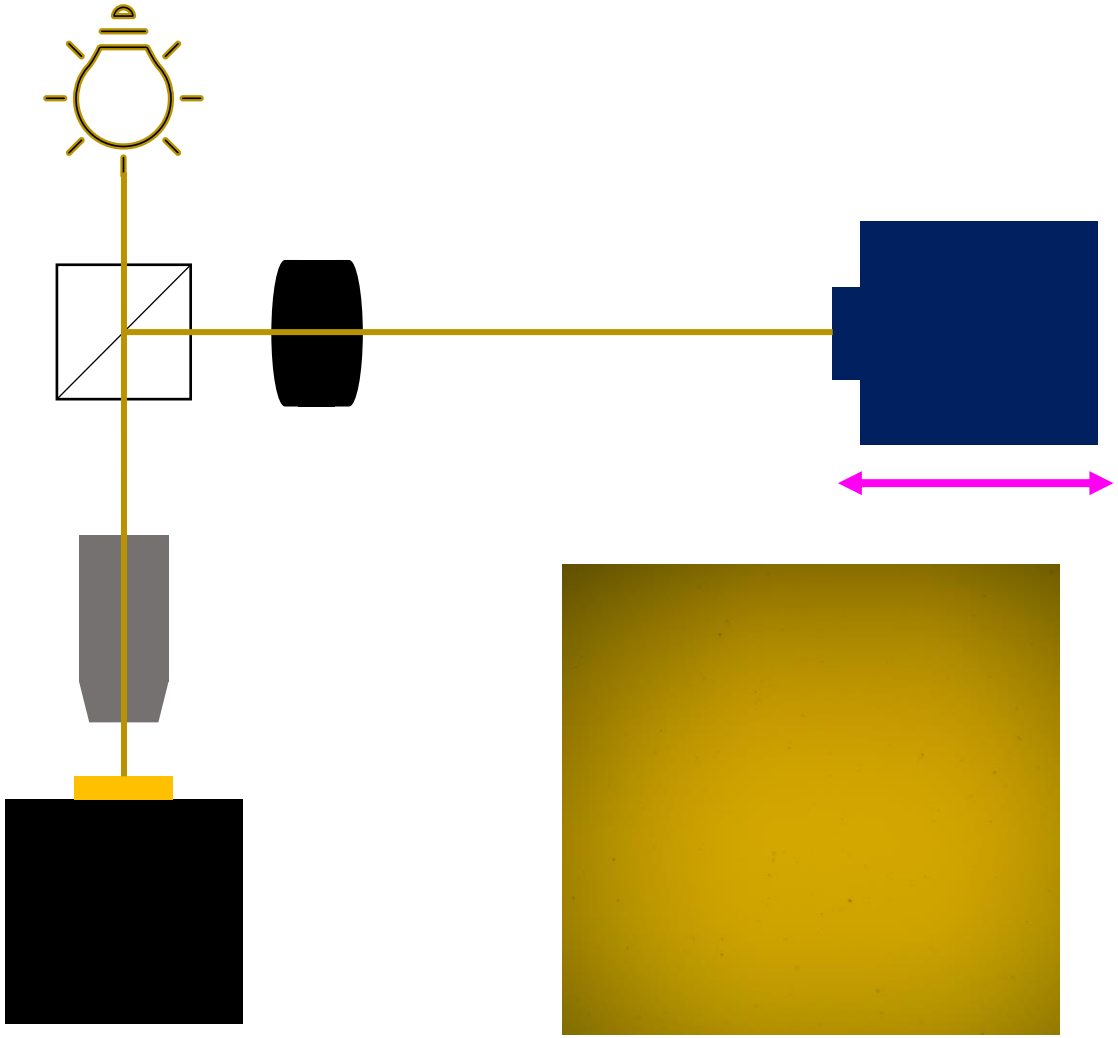

Camera Alignment and Sample Focusing – Procedure

Step 5: After iterating several times, the probe focus and the sample focus will converge to be optimal at the same place

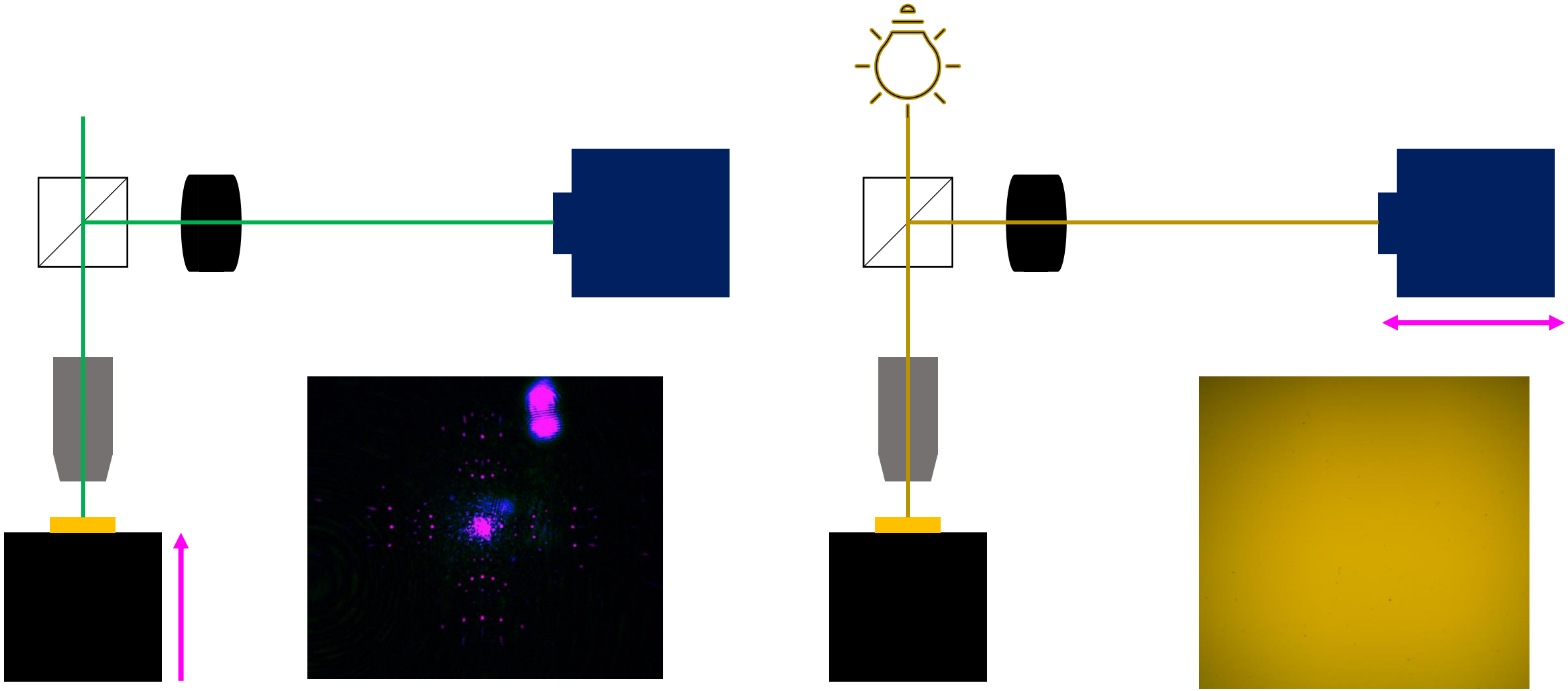

Laser Alignment Through the Objective

Depending on which microscope objective lens is chosen for the setup, aligning the beams through the objective without beam clipping can be challenging

Mitutoyo Long Working Distance (WD) Objective 20X

- Length = 75 mm
- WD = 20 mm
- Entrance Pupil = 8.4 mm

→ Longer objective housing means the beams can be clipped if only slightly misaligned, but with the benefit of longer WD

Olympus RMS20X

- Length = 43.7 mm
- WD = 1.2 mm
- EP = 7.2 mm

→ Easier to align through since the objective itself is shorter, but much less WD

TOP VIEW

Step 1: Ensure incoming probe beam is optimally aligned by iterating between Mirror 1 and Mirror 2 to align to points 1 and 2, respectively.

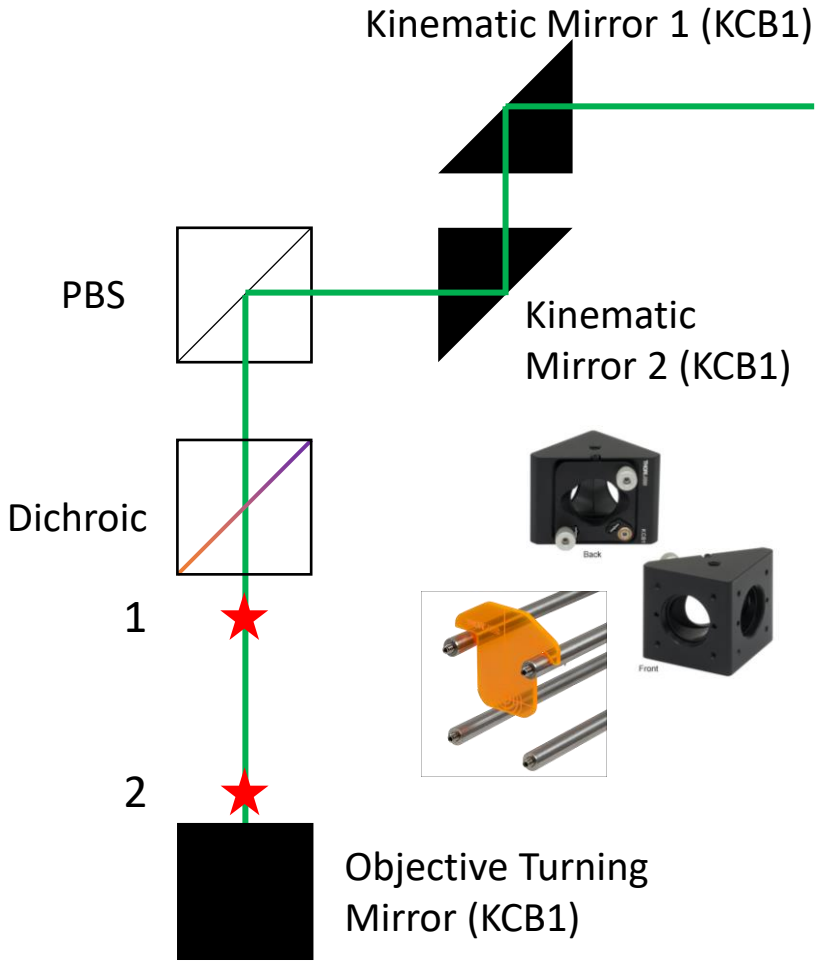

FRONT VIEW

Step 2: Use objective turning mirror to center beam through the objective column at points 3 and 4, respectively. Ensure it is centered all the way down. (objective is removed)

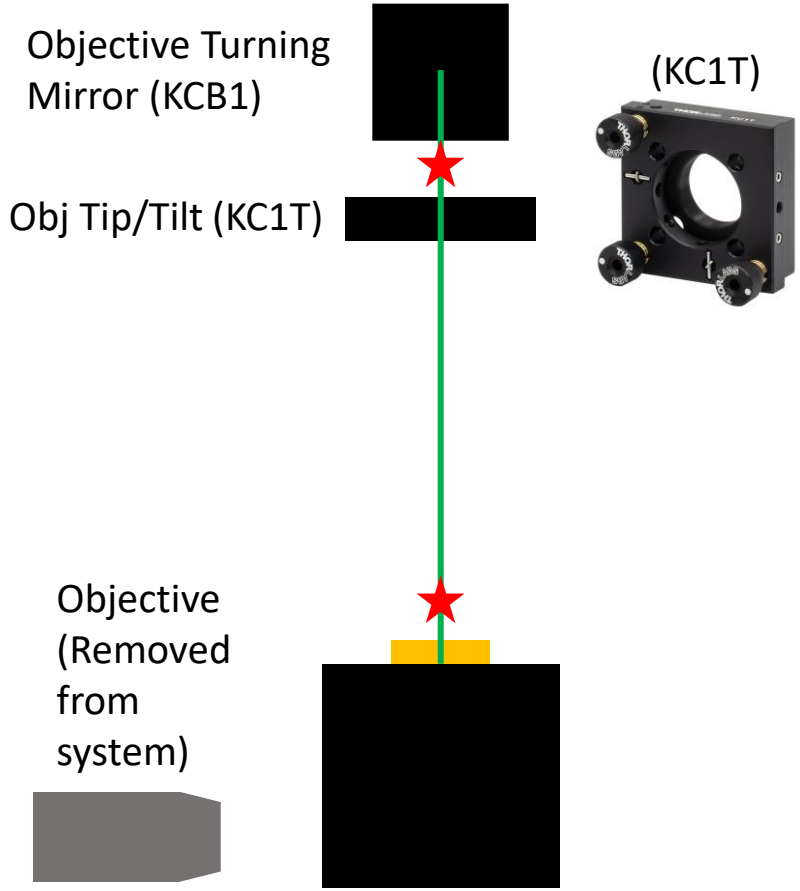

Laser Alignment Through the Objective

TOP VIEW

Step 3: Use tip/tilt/rotation mount to get back reflection from sample. Center on incoming beam at point 5. (objective still removed)

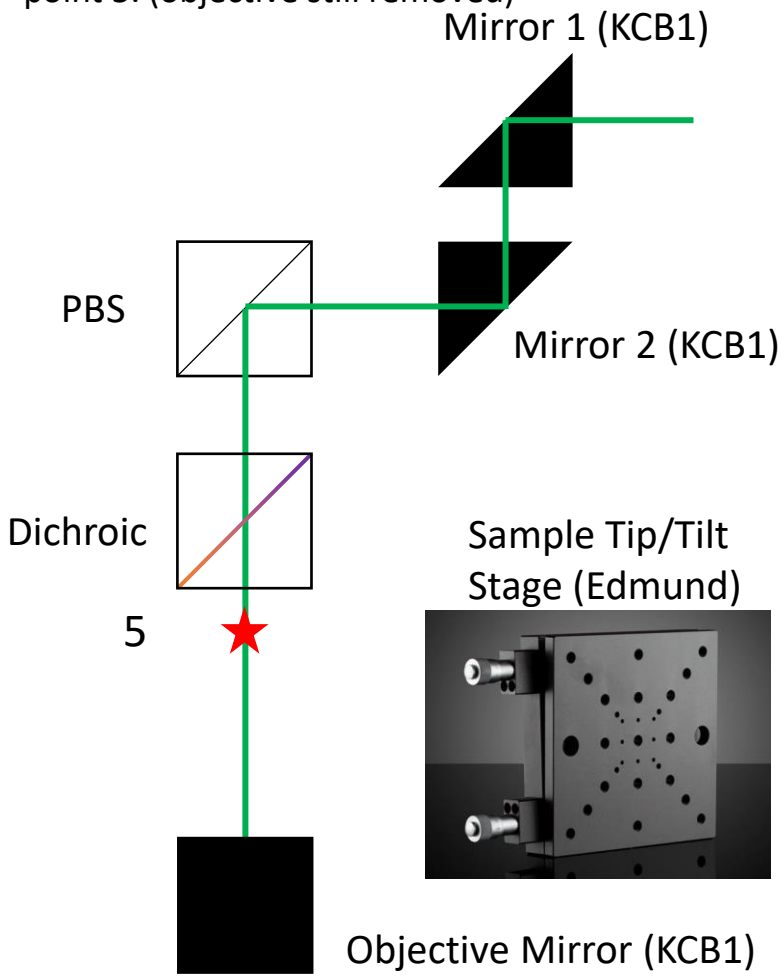

FRONT VIEW

Step 4: Mount mirror (using lens tube) on KC1T kinematic mount for objective to get back reflection from where objective goes. Align back reflection from objective to same point 5 for sample back reflection.

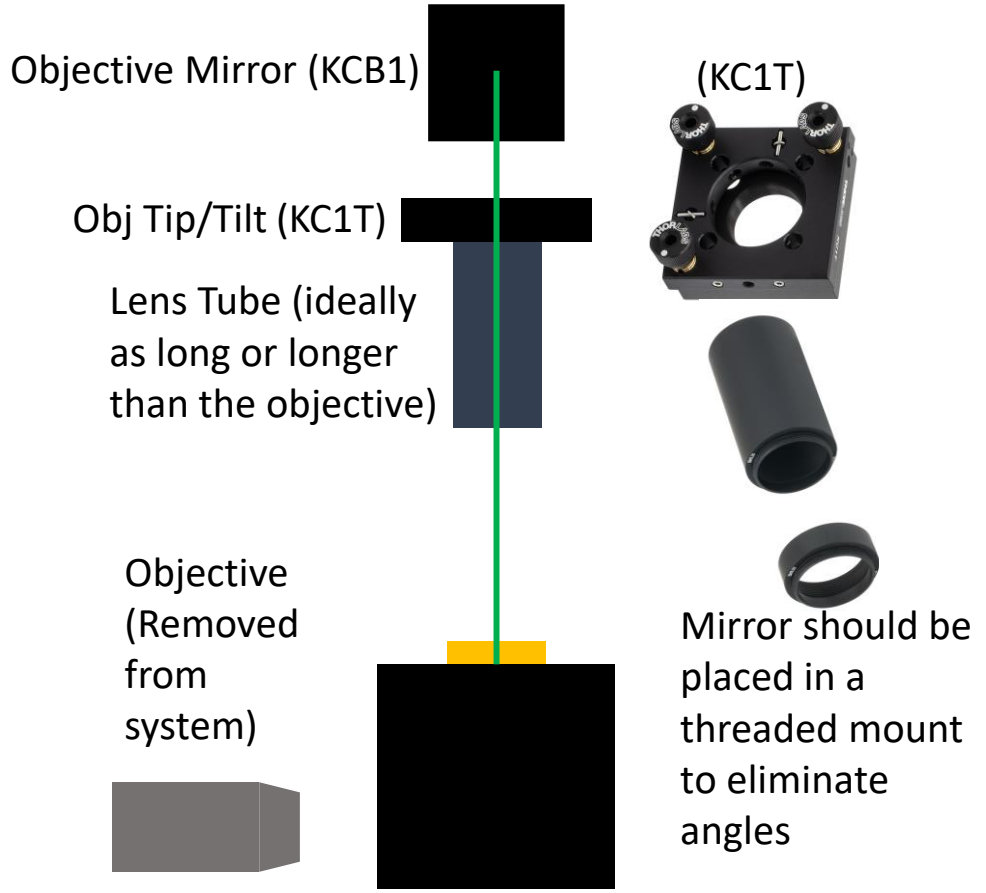

FRONT VIEW

Step 5: Mount Objective

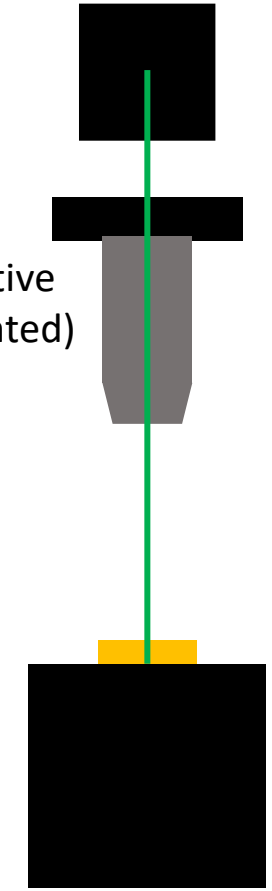

Alignment onto Detector

- **Kinematic mirror helps steer post-sample probe beam is the PD+ detector**
- Plano-convex lens (better for focusing collimated beams) or biconvex lens (better for focusing diverging beams)
  - **Mount lenses on a translation stage to control focused spot size on the detector and find optimal DC Voltage signal**
  - A lens kit is helpful to find the ideal focal length & lens position for the probe beam size and divergence
- Bandpass filter placed before the lens to block the reflected post-sample pump beam
- **Unoptimized placement of these lenses can lead to low frequency phase scatter or aberrant frequency dependence in the measured phase**
- Position of the probe detector lens must be readjusted to minimize the beam on the detector each time there is any movement in the objective, and only after verifying that the sample is in the objective focal plane

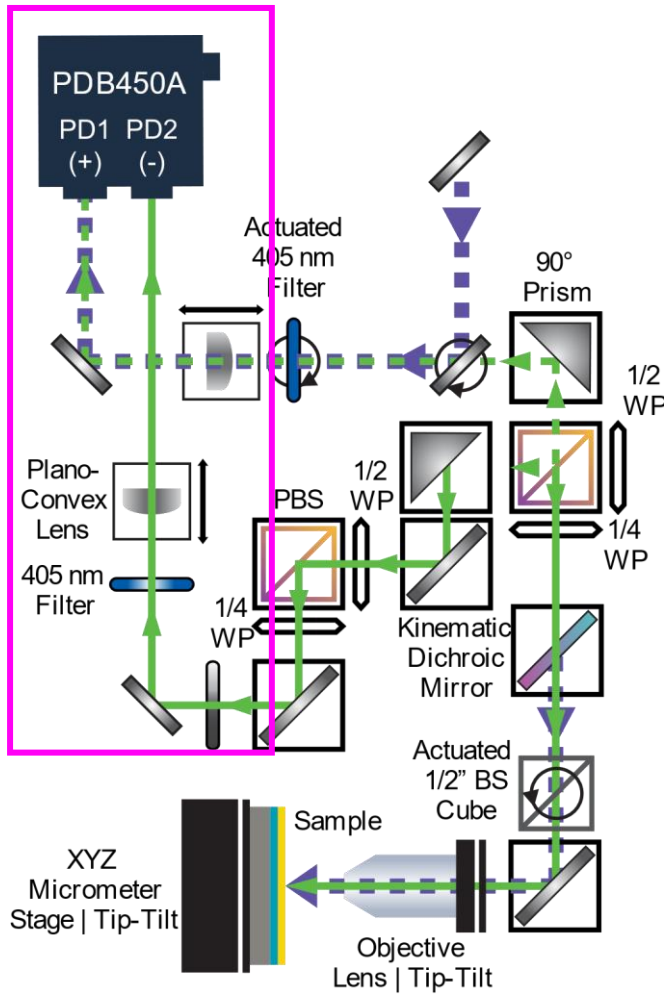

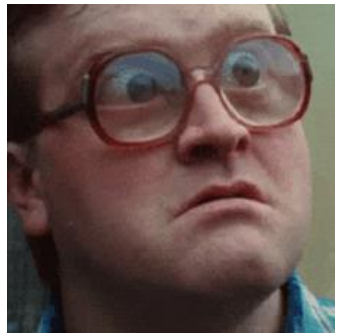

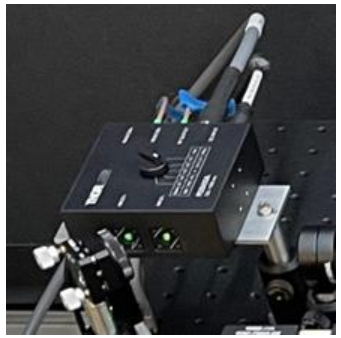

For sapphire (incident pump power ≈ 10 mW measured at 1 MHz); calculated temperature rise is ≈ 8.5 K at 100 Hz, ≈ 2.5 K at 1 MHz, and ≈ 0.7 K at 20 MHz. This produces a PD+ voltage of ≈ 4.7 V and a R magnitude measured by the LIA of > 1 mV at 100 Hz, ≈ 500 µV at 1 MHz, and ≈ 100 µV at 20 MHz.

D. Kirsch, J. Martin et al., Rev. Sci. Instrum. 95, 103006 (2024)

Electronics and Noise

- Standard signal cable connecting detector RF output and the HF2LI lock-in signal input resulted in measured phase deviations upwards of 1 ° to 2 ° if the cable was slightly moved, touched, or even if someone stood in proximity
  - **Ultra-low loss phase-stable cable performed much better with little phase deviation (8mm outer diameter)**
    - Use preset SMA torque wrench to properly tighten the connection on the back of the BPD
      - Over or under tightening can result in a degraded signal and affect the measured phase on the LIA
    - No drift or shift in phase is observed using this cable even when physically bending the cable or with changes in ambient temperature.
- **Tripp Lite Isobar Surge Protector used to isolate all instrumentation**[ref elbara]
  - High-frequency capacitors and toroidal balanced chokes remove noise interference, ferrite-core inductors suppress noise, and isolated filter banks block interference between connected devices (ground loops)
- **Hinged ferrites clamped on all power and signal cables**
  - ***Material 31*** cores (a newer Mn-Zn alloy) designed specifically for electromagnetic interference suppression from as low as 1 MHz.
  - **Ferrite cores clamped on pump modulation cable and the LIA input cable (near the inputs) produce the most significant reduction in phase noise in the high-frequency data**

Hinged ferrite clamped on the ultra-low loss phase stable cable connecting the BPD and LIA.

D. Kirsch, J. Martin et al., Rev. Sci. Instrum. 95, 103006 (2024)

Electronic Noise & Phase Noise

(Top) TR signal voltage magnitude (R_{TR}) compared with electronic noise voltage magnitude (R_{noise})

- Probe and pump beams blocked and the pump laser emitting and modulated
- Noise is negligible in broadband region but increases below ≈ 1000 Hz and increases slightly above ≈ 5 MHz
- The combination of noise density in the HF2LI lock-in amplifier and in the balanced photodiode electronics gives rise to the frequency dependence
- Below ≈ 10^4 Hz to ≈ 10^5 Hz, the noise density of balanced photodiodes operational amplifiers and transimpedance amplifier (TIA) decreases as the frequency increases ($1/f$)
- For TIA noise density then increases with frequency typically ≈ 1 MHz to ≈ 10 MHz (capacitive influences in TIA)

(Bottom) Phase noise in comparison with the absolute corrected phase lag data

- Phase noise density is given by $[S(V)/R]\sqrt{BW}$, in radians
  - $S(V)$ is the range dependent input voltage noise density (see Figure 9.6 in the HF2LI User Manual)
  - R is the measured rms voltage amplitude
  - BW is the bandwidth
- Bandwidth indicates cutoff frequency and is inversely related to the time constant by $BW=FO(2\pi\tau)$, where FO is the filter order prefactor and τ is the time constant

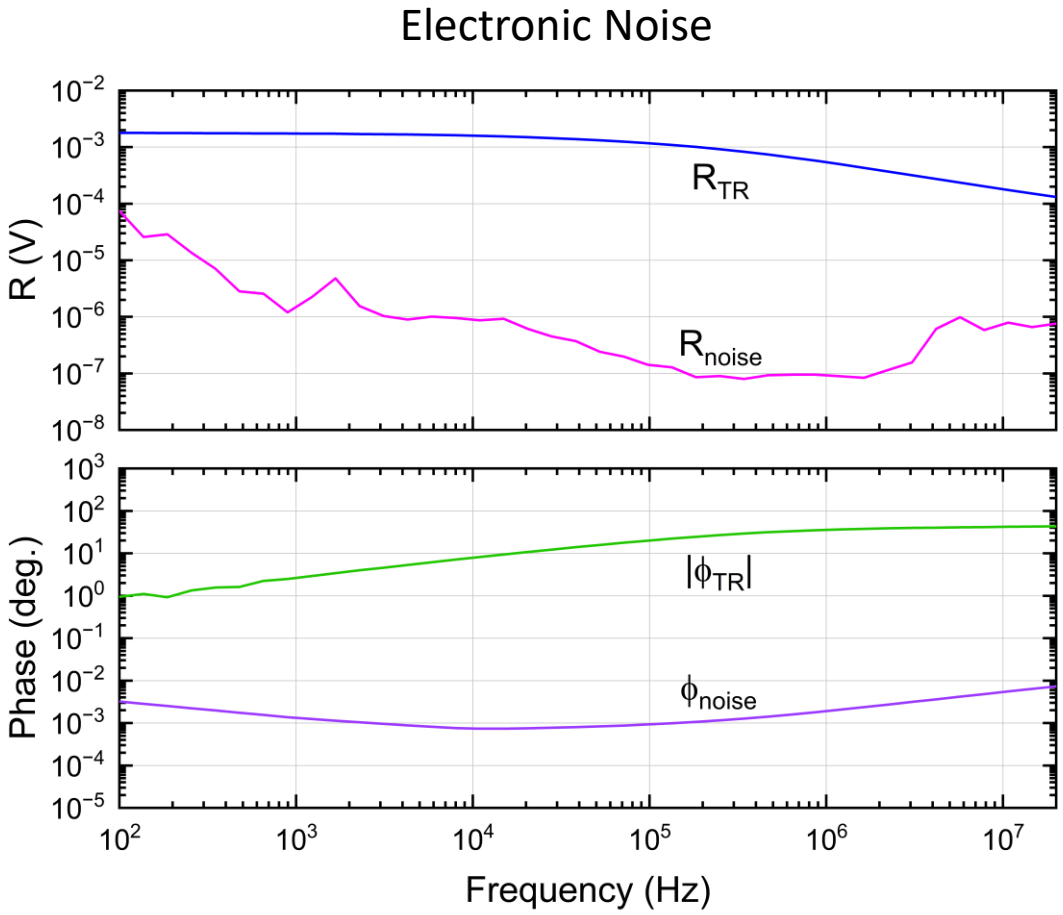

D. Kirsch, J. Martin et al., Rev. Sci. Instrum. 95, 103006 (2024)

Phase Standard Deviation

The frequency dependent standard deviation from representative phase measurements on 4 materials in comparison with the phase noise:

- Standard deviation is an output from the lock-in amplifier sweeper module using the number of data samples per sweeper parameter point averaged over the defined period of time considered in the measurement
- Standard deviation incorporates uncertainty components from the HF2LI phase noise density, the laser electronics, the balanced photodetector electronics, and the TR measurement
- The frequency dependence is due to the decrease in signal (*R*) with frequency, in combination with the noise in the HF2LI electronics and the balanced photodiode electronics
- The frequency averaged standard deviation is used as the phase measurement standard uncertainty component (± 0.1 °) in the Monte Carlo simulations

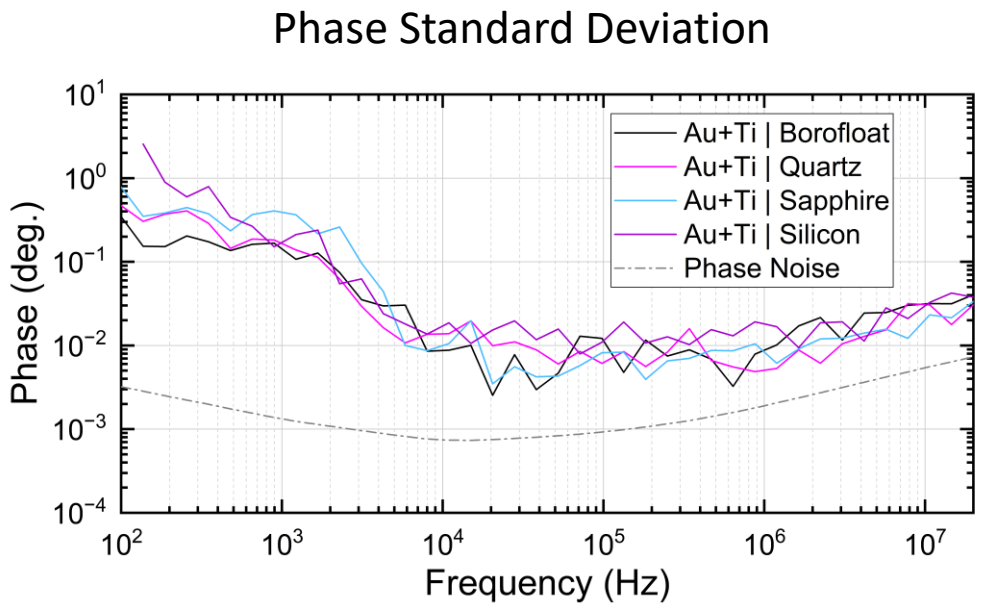

D. Kirsch, J. Martin et al., Rev. Sci. Instrum. 95, 103006 (2024)

Recommended Lock-in Settings

Commands	Value	Unit
sweep/filtermode	1 (Advanced)	—
sweep/start	100	Hz
sweep/stop	2×10^{7}	Hz
sweep/samplecount	40	—
sweep/settling/time	1 - 5	s
sweep/omegasuppresion	120	dB
sweep/averaging/sample	100 [b]	—
sweep/averaging/tc	25 – 100 [b,c]	—
sweep/averaging/time	1 [b]	s
sweep/bandwidthcontrol	2 (Auto) [d]	—
sweep/bandwidthoverlap	1 (On)	—
sweep/phaseunwrap	1 (On)	—
sweep/scan	0 (Sequential)	—
sweep/settling/inaccuracy	1×10^{-14}	—
sweep/xmapping	1 (Log)	—
sweep/maxbandwidth	1	Hz
sweep/order	8	—

[b] The maximum between samples, time and number of time constants is taken as effective calculation time.
[c] This value is a multiplier (×TC)
[d] For these settings, the bandwidth and the time constant remain the same for all sweep frequencies even with auto bandwidth control enabled.

While other lock-in settings may affect the total measurement time, the bandwidth is the primary determinate of the measurement standard deviation

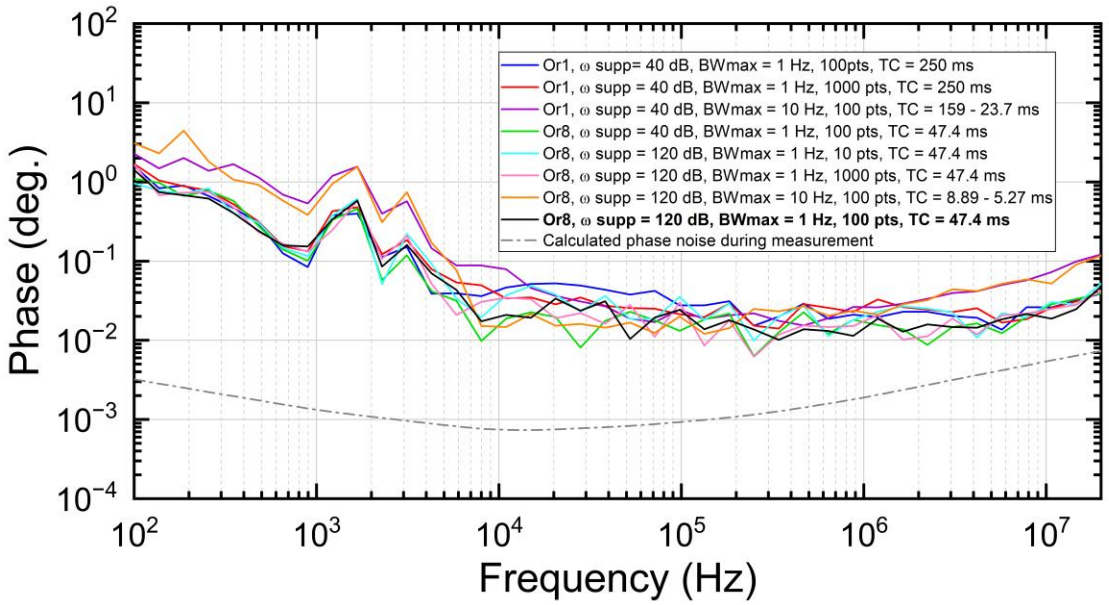

D. Kirsch, J. Martin et al., Rev. Sci. Instrum. 95, 103006 (2024)

FDTR Thermal Model: Custom MATLAB GUI

- Custom, user-friendly MATLAB App Designer GUI created to simplify FDTR data plotting, correction, and fitting
- **Initial (rapid) fitting of the measured phase data to the multilayer thermal model accomplished using the MATLAB nlinfit nonlinear regression fitting function** with MATLAB nlparci fit uncertainty
- **Robust uncertainty analysis for the extracted best fit thermal model parameters performed via a Monte Carlo fitting approach** (generates N random sets of input parameter values within the input parameter uncertainty to run the fitting routine)
  - **Uses least squares nonlinear regression (MATLAB lsqcurvefit)**
  - **Mean extracted thermal model fit value for a parameter determined by a normal distribution fit of the array of Monte Carlo fit values**

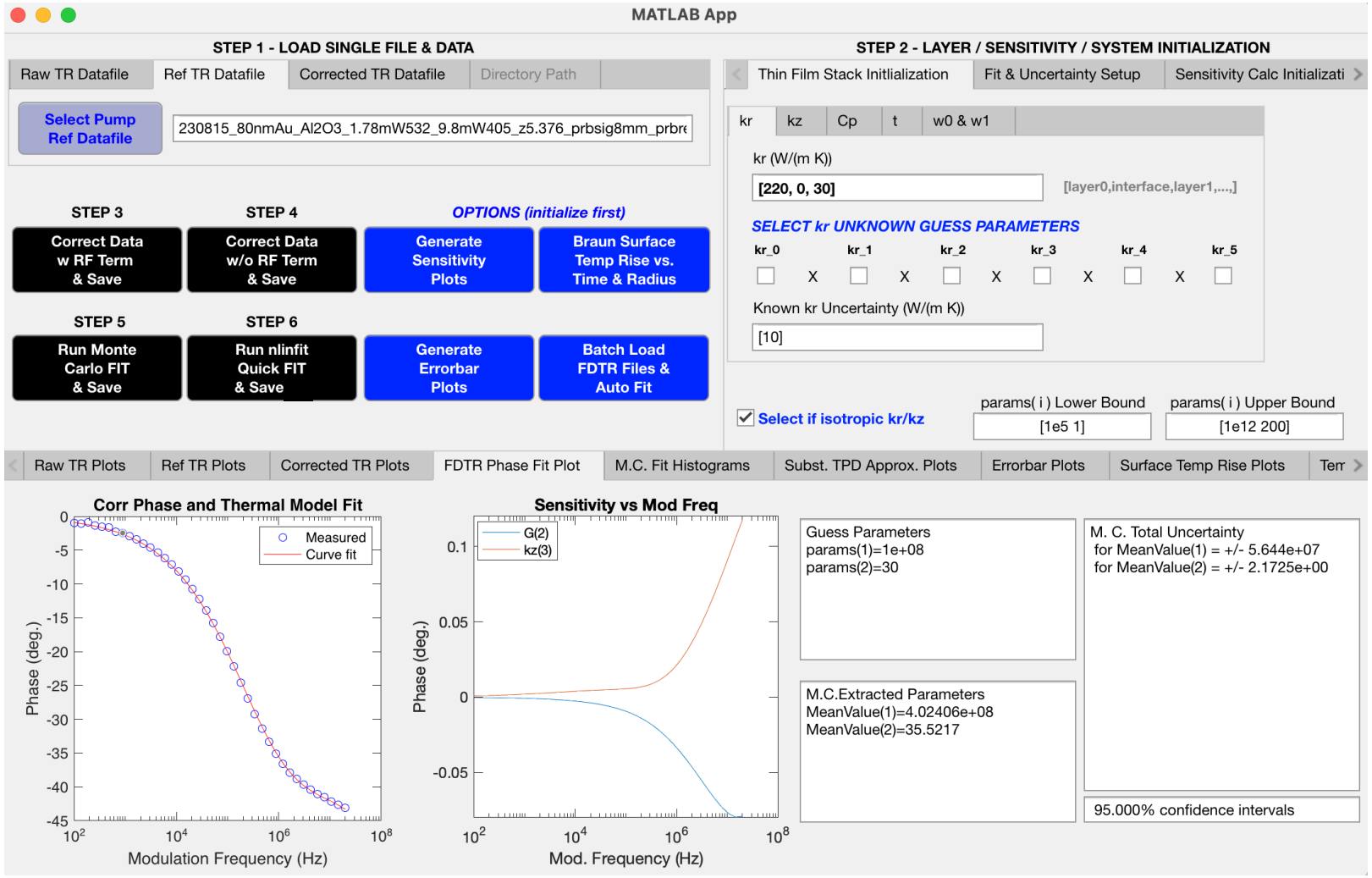

$$\phi = \tan^{-1}\frac{\Im\left(\mathbf{H}(r,\omega)\right)}{\Re\left(\mathbf{H}(r,\omega)\right)} + \phi_{ext}$$

$$H(\omega) = \frac{1}{2\pi}\int_0^\infty k\left(\frac{-D}{C}\right)\exp\left[\frac{-k^2(w_0^2+w_1^2)}{8}\right]dk$$

D. Kirsch, J. Martin et al., Rev. Sci. Instrum. 95, 103006 (2024)

Numerical Integration

$$H(\omega) = \frac{1}{2\pi}\int_0^{\infty} k\left(\frac{-D}{C}\right)\exp\left[\frac{-k^2(w_0^2 + w_1^2)}{8}\right]dk$$ Evaluate over [0,L]→ $L = m/\sqrt{(w_0^2 + w_1^2)}$

Computational results and times for a Au+Ti | Sapphire sample comparing Gauss–Legendre quadrature (using lgwt) and trapezoidal integration (using trapz)

- Isotropic thermal conductivity values obtained using trapezoidal numerical integration are consistent with the those obtained using Gauss–Legendre quadrature using published recommended parameters
- Trapezoidal integration may require fewer integration points and less computational time
- Trapezoidal numerical integration is likely more sensitive to truncation than Gauss–Legendre quadrature and larger upper limits should be used
- Gauss–Legendre quadrature is likely more sensitive to point density
- Gauss–Legendre quadrature with an extended interval limit require substantially more computational time to converge
- In a Monte Carlo simulation, the computational time will scale with the number of iterations (1000 in our implementation)
    - In the higher interval limit regime, using the trapezoidal method can decrease the MC computational time from ≈ 7 hrs. to ≈ 30 min

MATLAB Function	N	m	Lower k-value Limit (m^{-1})	Upper k-value Limit (m^{-1})	Computational Time (s)	k_{iso} (W m^{-1} K^{-1})
trapz	75	10^4	10^2	10^9	1.55 ± 0.01	35.6518 ± 0.6091
	400	10^4	10^2	10^9	7.80 ± 0.03	35.6518 ± 0.6091
	1000	10^4	10^2	10^9	19.40 ± 0.05	35.6518 ± 0.6091
	75	16	10^2	10^6	1.51 ± 0.07	35.6926 ± 0.6020
	400	16	10^2	10^6	5.68 ± 0.05	35.6834 ± 0.6036
	600	16	10^2	10^6	8.50 ± 0.09	35.6832 ± 0.6036
	1000	16	10^2	10^6	14.12 ± 0.10	35.6831 ± 0.6036
lgwt	75	16	≈ 10^2	≈ 2×10^6	1.53 ± 0.09	35.6518 ± 0.6091
	100	10	≈ 10^2	≈ 1×10^6	2.00 ± 0.08	35.6519 ± 0.6092
	100	16	≈ 10^2	≈ 2×10^6	1.98 ± 0.10	35.6518 ± 0.6091
	400	16	≈ 10^2	≈ 2×10^6	8.27 ± 0.24	35.6518 ± 0.6091
	75	10^4	≈ 10^2	≈ 10^9	—	—
	400	10^4	≈ 10^2	≈ 10^9	9.46 ± 0.13	35.7721 ± 1.1307
	600	10^4	≈ 10^2	≈ 10^9	13.43 ± 0.08	35.6295 ± 0.6212
	1000	10^4	≈ 10^2	≈ 10^9	24.09 ± 0.07	35.6518 ± 0.6150
	1500	10^4	≈ 10^2	≈ 10^9	30.18 ± 0.07	35.6519 ± 0.6090

The mean best fit isotropic thermal conductivity value (using the MATLAB nlinfit function), the computational time, and the expanded uncertainties (with a normal distribution coverage factor k = 2 for an approximately 95.45% coverage probability) were determined using 10 sequential calculations. The number of significant figures is expanded for clarity. Numerical integration truncates the interval [0, L], where the upper limit $L=m/(w_0^2+w_1^2)$ and typically $2 \le m \le 16$. The lower interval limit is 0 for all cases. For Gauss–Legendre quadrature, the interval upper limit and the number of integration points were selected according to Braun *et al.*[1] and Ziade.[2] For trapezoidal numerical integration, we generate the k vector as 75 log-spaced points in a wider interval between 10^2 m^{-1} and 10^9 m^{-1} using $m = 10^4$ (integration numbers below 50 results in diverging unknown fit parameter values).

D. Kirsch, J. Martin et al., Rev. Sci. Instrum. 95, 103006 (2024)

"A referee asks, do the themes we have discussed lead to any advice on how to select the right quadrature formula for an application? Perhaps the advice is that if you are told that a certain formula is optimal, do not assume this is the end of the discussion."

-L. N. Trefethen, Exactness of Quadrature Formulas, SIAM Review Vol. 64, pp. 132-150 (2022)

Representative Data & Monte Carlo (MC) Histograms

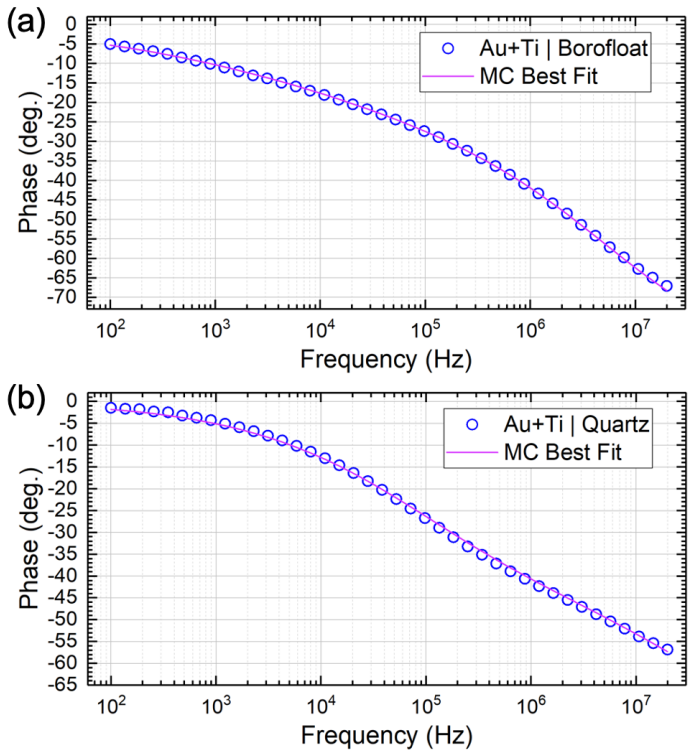

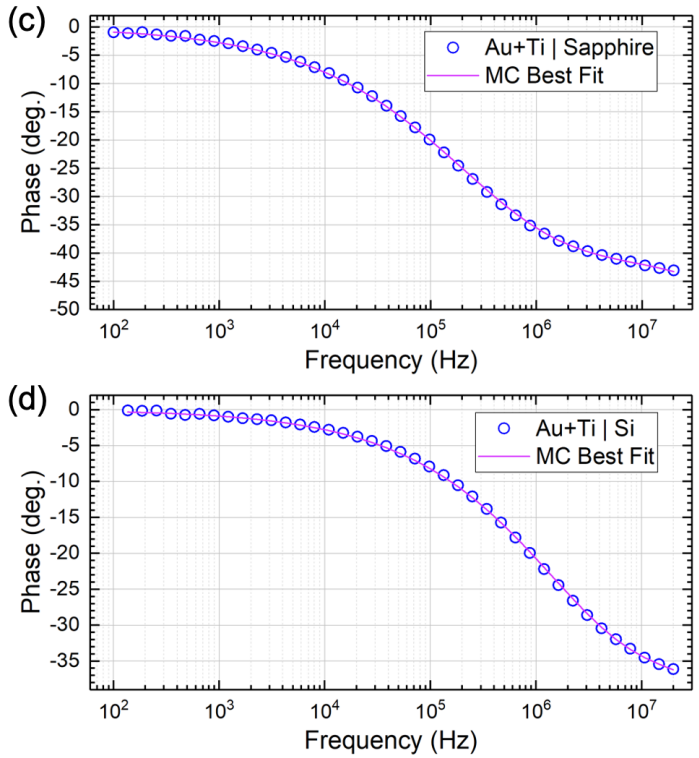

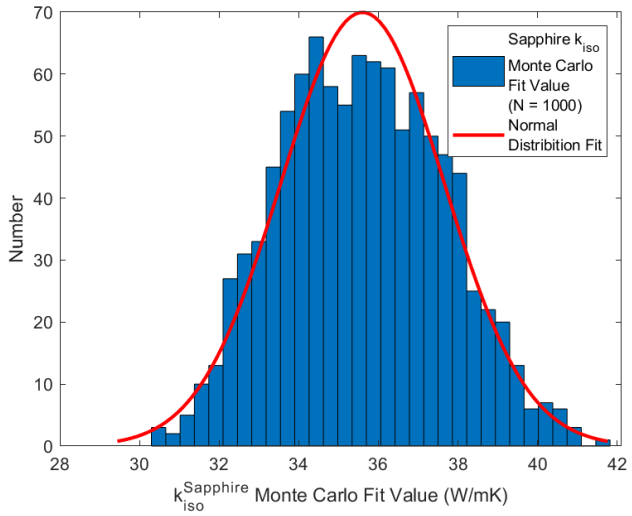

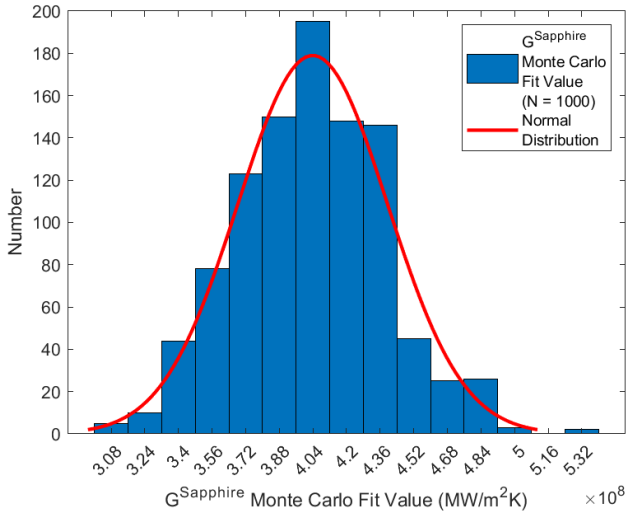

D. Kirsch, J. Martin et al., Rev. Sci. Instrum. 95, 103006 (2024)

Quick Fit & MC Fit Uncertainty Comparison

Compared two fitting approaches (both using trapezoidal numerical integration):

- nlinfit initial fit (computation time of ≈ 1 s)
  - FIT UNCERTAINTY ONLY: total expanded uncertainty ± kuc, where uc is the total combined uncertainty, (k = 2, ≈ 95.45 % coverage probability)
- 1000 iteration Monte Carlo simulation fit (computational time of ≈ 30 minutes) (including standard uncertainties in known fit parameters)
  - Standard uncertainty components include: transducer thickness, volumetric heat capacity, and isotropic thermal conductivity; substrate heat capacity (± 3 %); pump and probe spot size (± 0.2 µm and ± 0.1 µm, respectively); and phase standard deviation (± 0.1º)
- Total uncertainty expressed as the total expanded uncertainty ± kuc with a normal distribution factor k = 2 for an approximately 95.45 % coverage probability
- Initial fit and Monte Carlo fit values agree with each other and with reported literature values within the uncertainty
- Monte Carlo simulation relative total expanded uncertainties (≈ 7 % to ≈ 10 %) are larger than the initial fit relative total expanded uncertainties (≈ 2 % to ≈ 6 %) since they include the propagated standard uncertainties in the known parameters

			Initial Fitting		**Monte Carlo Simulation**	
	Reference Values		Unknown Fit Parameter 1	Unknown Fit Parameter 2	Unknown Fit Parameter 1	Unknown Fit Parameter 2
Material	C_V (MJ m^{-3} K^{-1})	κ_{iso} (W m^{-1} K^{-1})	κ_{iso} (W m^{-1} K^{-1})	G (MW m^{-2} K^{-1})	κ_{iso} (W m^{-1} K^{-1})	G (MW m^{-2} K^{-1})
Borofloat	1.85 ± 0.1 [78]	1.1 ± 0.07 [78]	1.21 ± 0.05	—	1.16 ± 0.11	—
Quartz	2.0 ± 0.2 [79]	8.15 ± 1.0 [79]	8.15 ± 0.5	—	8.21 ± 0.61	—
Sapphire	3.06 ± 0.1 [80]	35.5 ± 2 [81]	35.7 ± 0.6	400.4 ± 17.2	35.6 ± 2.6	403.9 ± 36.7
Silicon	1.66 ± 0.1 [82]	148 ± 8.6 [83]	156.3 ± 3.2	463.6 ± 25.3	154.4 ± 11.4	453.9 ± 52.2

D. Kirsch, J. Martin et al., Rev. Sci. Instrum. 95, 103006 (2024)

FDTR Instrument Guide Now Available!

An instrumentation guide to measuring thermal conductivity using frequency domain thermoreflectance (FDTR)

Cite as: Rev. Sci. Instrum. 95, 103006 (2024); doi: 10.1063/5.0213738
Submitted: 12 April 2024 • Accepted: 19 September 2024 •
Published Online: 14 October 2024

View Online Export Citation CrossMark

Dylan J. Kirsch,[1,2,a] Joshua Martin,[1,b] Ronald Warzoha,[3,c] Mark McLean,[1,d] Donald Windover,[1,e] and Ichiro Takeuchi[2,f]

AFFILIATIONS

[1] Material Measurement Laboratory, National Institute of Standards and Technology, Gaithersburg, Maryland 20899, USA
[2] Department of Materials Science and Engineering, University of Maryland, College Park, Maryland 20742, USA
[3] Department of Mechanical and Nuclear Engineering, United States Naval Academy, Annapolis, Maryland 21402, USA

[a] **Author to whom correspondence should be addressed:** dylan.kirsch@nist.gov
[b] joshua.martin@nist.gov
[c] warzoha@usna.edu
[d] mark.mclean@nist.gov
[e] donald.windover@nist.gov
[f] takeuchi@umd.edu

ABSTRACT

Frequency Domain Thermoreflectance (FDTR) is a versatile technique used to measure the thermal properties of thin films, multilayer stacks, and interfaces that govern the performance and thermal management in semiconductor microelectronics. Reliable thermal property measurements at these length scales (≈10 nm to ≈10 μm), where the physics of thermal transport and phonon scattering at interfaces both grow in complexity, are increasingly relevant as electronic components continue to shrink. While FDTR is a promising technique, FDTR instruments are generally home-built; they can be difficult to construct, align, and maintain, especially for the novice. Our goal here is to provide a practical resource beyond theory that increases the accessibility, replicability, and widespread adoption of FDTR instrumentation. We provide a detailed account of unpublished insights and institutional knowledge that are critical for obtaining accurate and repeatable measurements of thermal properties using FDTR. We discuss component selection and placement, alignment procedures, data collection parameters, common challenges, and our efforts to increase measurement automation. In FDTR, the unknown thermal properties are fit by minimizing the error between the phase lag at each frequency and the multilayer diffusive thermal model solution. For data fitting and uncertainty analysis, we compare common numerical integration methods, and we compare multiple approaches for fitting and uncertainty analysis, including Monte Carlo simulation, to demonstrate their reliability and relative speed. The instrument is validated with substrates of known thermal properties over a wide range of isotropic thermal conductivities, including Borofloat silica, quartz, sapphire, and silicon.

Published by AIP Publishing. https://doi.org/10.1063/5.0213738

https://pubs.aip.org/aip/rsi/article/95/10/103006/3316821/An-instrumentation-guide-to-measuring-thermal

Acknowledgements

Tremendous thank you to:

- **NSF GRFP**
- **UMD Clark Doctoral Fellowship**
- **Prof. Ichiro Takeuchi (UMD)**
- **Dr. Joshua Martin (NIST)**
- **Prof. Ron Warzoha (USNA)**
- **Dr. Mark McLean (NIST)**
- **Dr. Donald Windover (NIST)**
- **Dr. Apurva Mehta (SLAC)**
- **NIST NanoFab**

NIST MATERIAL MEASUREMENT LABORATORY

U.S. DEPARTMENT OF ENERGY | Energy Efficiency & Renewable Energy

ADVANCED MANUFACTURING OFFICE

Contract #DE-ACO2-76-SF00515

NSF GRFP

UNIVERSITY OF MARYLAND 18 56

SLAC NATIONAL ACCELERATOR LABORATORY

CHIPS for AMERICA

DARPA

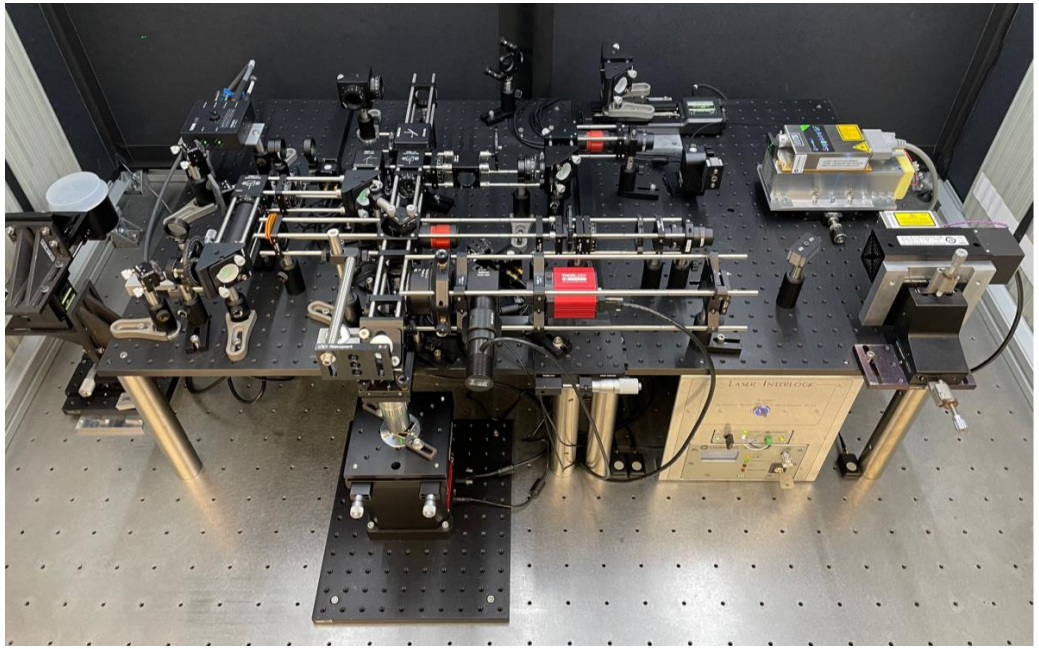

D. Kirsch, J. Martin et al., Rev. Sci. Instrum. 95, 103006 (2024)

Supplementary Information – TIA and Op-Amp Noise Characteristics

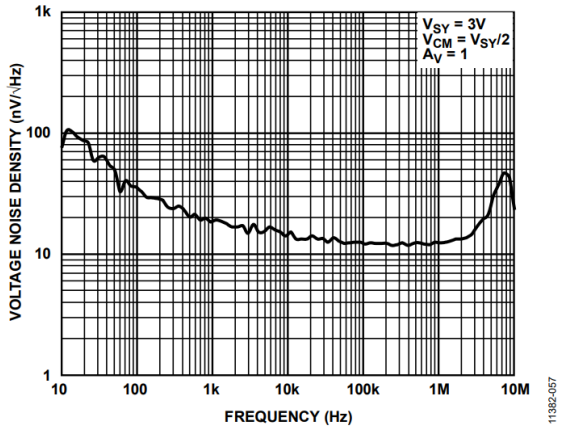

Figure 56. Voltage Noise Density vs. Frequency

The small increase in electronic noise voltage magnitude above ≈ 5 MHz arises from the balanced photodiode electronics. The balanced photodiode contains several Operational Amplifiers (Op-Amps) and a transimpedance amplifier. The noise density frequency dependence of these electronic components are well understood and match the dependence shown in Figure S9. Below ≈ 10^4 Hz to 10^5 Hz, the noise density of these electronic components decreases as the frequency increases then increases with frequency typically beginning around 1 MHz to 10 MHz. See for example Figure 56 and Figure 59 for a common Op-Amp: https://www.analog.com/media/en/technical-documentation/data-sheets/ADA4666-2.pdf,

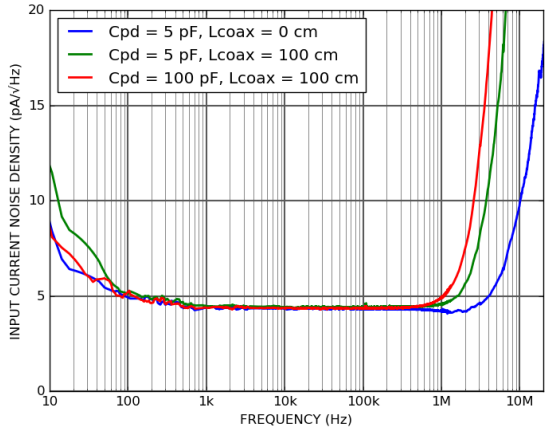

The increase is especially notable in transimpedance amplifiers, where the additional capacitive components directly influence the specific frequency range of the noise increase, for example: https://www.koheron.com/photonics/tia100-transimpedance-amplifier

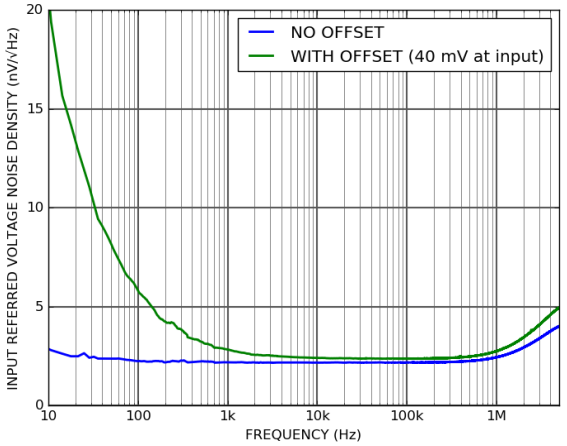

the AMP200-10k voltage preamplifier (figure at bottom): https://www.koheron.com/photonics/amp200-amplifier,

and the Thorlabs TIA60:

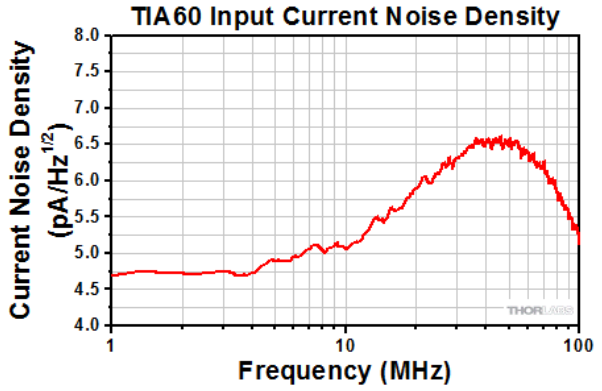

https://e2e.ti.com/support/amplifiers-group/amplifiers/f/amplifiers-forum/586219/opa847-voltage-noise-peaking-in-transimpedance-amplifier-tia---why-does-the-addition-of-a-feedback-capacitor-cause-voltage-noise-peaking